Reaction Landscape of a Mononuclear Mn(III)-hydroxo Complex with Hydrogen Peroxide

Journal:	*Dalton Transactions*
Manuscript ID	DT-ART-08-2023-002672.R1
Article Type:	Paper
Date Submitted by the Author:	08-Sep-2023
Complete List of Authors:	Grotemeyer, Elizabeth; University of Kansas College of Liberal Arts and Sciences, Chemistry Parham, Josh; University of Kansas College of Liberal Arts and Sciences, Chemistry Jackson, Timothy; University of Kansas College of Liberal Arts and Sciences, Chemistry

Reaction Landscape of a Mononuclear Mn^{III}-hydroxo Complex with Hydrogen Peroxide

Elizabeth N. Grotemeyer, Joshua D. Parham†, and Timothy A. Jackson*

The University of Kansas, Department of Chemistry and Center for Environmentally Beneficial Catalysis,
1567 Irving Hill Road, Lawrence, KS 66045, USA.

*To whom correspondence should be addressed:
Timothy A. Jackson
Phone: (785) 864-3968
taj@ku.edu

†Current address: Department of Physical Sciences, University of Central Missouri, Warrensburg, MO 64093.

Abstract

Peroxomanganese species have been proposed as key intermediates in the catalytic cycles of both manganese enzymes and synthetic catalysts. However, many of these intermediates have yet to be observed. Here, we report the formation of a series of intermediates, each generated from the reaction of the mononuclear Mn^{III}-hydroxo complex [Mn^{III}(OH)(dpaq^{2Me})]$^+$ with hydrogen peroxide under slightly different conditions. By changing the acidity of the reaction mixture and/or the quantity of hydrogen peroxide added, we are able to control which intermediate forms. Using a combination of electronic absorption, ^{1}H NMR, EPR, and X-ray absorption spectroscopies, as well as density functional theory (DFT) and complete active space self-consistent field (CASSCF) calculations, we formulate these intermediates as the bis(μ-oxo)dimanganese(III,IV) complex [Mn^{III}Mn^{IV}(μ-O)$_2$(dpaq^{2Me})$_2$]$^+$, the Mn^{III}-hydroperoxo complex [Mn^{III}(OOH)(dpaq^{2Me})]$^+$, and the

Mn^{III}-peroxo complex [Mn^{III}(O$_2$)(dpaq^{2Me})]. The formation of the Mn^{III}-hydroperoxo species from the reaction of a Mn^{III}-hydroxo complex with hydrogen peroxide mimics an elementary reaction proposed for many synthetic manganese catalysts that activate hydrogen peroxide.

Introduction

Manganese enzymes that react with oxygen or its derivatives are commonly proposed to form peroxo intermediates as part of their catalytic cycles.[1-2] For example, the formation of a dinuclear bis(μ-oxo)diamanganese(III,IV) species in Mn-ribonucleotide reductase (Mn-RNR) from superoxide and a dimanganese(II,II) form of the enzyme is proposed to proceed through a Mn^{III}-peroxo intermediate.[3-6] For Mn-dependent dioxygenases and Mn-lipoxygenases, it has been proposed that O$_2$-derived Mn-alkylperoxo intermediates form during substrate oxidation.[7-11] The product-inhibited complex of manganese superoxide dismutase, which forms under high superoxide concentration, is presumed to be a Mn^{III}-peroxo adduct,[12-14] but the exact nature of this species (i.e. side-on Mn^{III}-peroxo versus end-on Mn^{III}-hydroperoxo complex) is a matter of contention.[15-17] Water oxidation by the oxygen evolving complex of Photosystem II could result in the formation of a putative Mn-OO(H)-M intermediate (M = Mn or Ca) during O-O bond formation.[18-23] Despite the prevalence of peroxo intermediates among manganese enzymes, the majority of these proposed intermediates have not been observed.

Many synthetically useful manganese catalysts that activate H$_2$O$_2$ have also been proposed to utilize peroxo intermediates as part of their catalytic cycles.[24-28] These catalysts have been used for a variety of oxidation reactions, including sulfoxidation[29] and C-H hydroxylation;[30-34] however, these catalysts are most widely used in olefin epoxidation reactions due to their high efficiencies and remarkable selectivity in asymmetric epoxidations.[24, 30, 35-43] Mechanistic studies indicate that the active catalytic species in these reactions is a Mn^{V}-oxo species produced via heterolytic O-O cleavage of a Mn^{III}-hydroperoxo intermediate.[43-48] This cleavage is often facilitated by a carboxylic acid, such as acetic acid, that hydrogen bonds with the hydroperoxo ligand. This mechanism has been supported by kinetic analyses[30, 49] and labelling experiments[34, 46, 48] as well as by computational studies.[26, 30] As has been the case with enzymatic systems, neither the Mn^{V}-oxo active species nor the Mn^{III}-OOH precursor have been observed directly.

The importance of peroxo-level intermediates in catalytic and biological pathways has led to the development of synthetic model complexes as investigative tools. While there have been numerous examples of synthetic side-on Mn^{III}-peroxo species,[50-65] examples of end-on Mn^{III}-hydroperoxo or Mn-alkylperoxo complexes are rare.[66-73] Reports investigating reactivity of Mn^{III}-hydroperoxo complexes are especially limited, with only a handful of examples having been reported.[66-69] The formation of the Mn^{III}-hydroperoxo complexes $[Mn^{III}(OOH)(14\text{-TMC})]^{2+}$ and $[Mn^{III}(OOH)(13\text{-TMC})]^{2+}$ was achieved through the addition of perchloric acid to their side-on Mn^{III}-peroxo counterparts in MeCN at -40 °C (14-TMC = 1,4,8,11-tetramethyl-1,4,8,11-tetraaza-cyclotetradecane, 13-TMC = 1,4,8,11-tetramethyl-1,4,8,11-tetraaza-cyclotridecane).[67] The Mn^{III}-hydroperoxo complexes were characterized by electronic absorption, resonance Raman, electron paramagnetic resonance (EPR), and X-ray absorption spectroscopy.[66-67] These complexes were only stable at -40 °C, and rapidly carried out oxygen atom transfer (OAT) reactions with thioanisole and its derivatives at this temperature.[66-67] In addition to OAT reactivity, $[Mn^{III}(OOH)(13\text{-TMC})]^{2+}$ was also capable of performing hydrogen atom transfer (HAT) reactions with hydrocarbons with weak C-H bonds, including xanthene, 9,10-dihydroanthracene (DHA), and 1,4-cyclohexadiene.[66] Aldehyde deformylation of cyclohexane carboxaldehyde by $[Mn^{III}(OOH)(13\text{-TMC})]^{2+}$ was also observed.[66] Additional manganese(III)-hydroperoxo species have been reported by Lin et al.[68-69] In this case, $[Mn^{III}(OOH)(BDPP)]$ (H_2BDPP = 2,6-bis((2-(S)-

diphenylhydroxylmethyl-1pyrrolidinyl)methyl)pyridine) and [Mn^{III}(OOH)(BDP^{Br}P)] (H_2BDP^{Br}P = 2,6-bis((2-(S)-di(4-bromo)phenylhydroxylmethyl-1pyrrolidinyl)methyl)pyridine) were generated from Mn(BDPP)-superoxo and Mn(BDP^{Br}P)-superoxo species after a HAT reaction with TEMPOH (TEMPOH = 2,2′-6,6′-tetramethylpiperidine-1-ol). These complexes were characterized by electronic absorption and EPR spectroscopies.[69] [Mn^{III}(OOH)(BDP^{Br}P)] could also be produced by the one-electron reduction of the corresponding Mn^{IV}-OOH species.[68] Reactivity of [Mn^{III}(OOH)(BDPP)] and [Mn^{III}(OOH)(BDP^{Br}P)] towards substrates was not reported.

While these studies have provided insight into the properties of Mn^{III}-hydroperoxo complexes, these compounds failed to show reactivity most pertinent to manganese catalysts. In addition, these complexes are not generated by direct reaction of a manganese(III) center with H_2O_2, as is presumed for H_2O_2-activating manganese catalysts.[24-25, 43-45] In this work, we attempt to mimic this chemistry by exploring the reaction of the mononuclear Mn^{III}-hydroxo complex [Mn^{III}(OH)(dpaq^{2Me})]$^+$ with H_2O_2 under different reaction conditions (Hdpaq^{2Me} = 2-[bis(pyridin-2-ylmethyl)]aminoN-2-methyl-quinolin-8-yl-acetamidate). We report the formation and characterization of a series of products, [Mn^{III}Mn^{IV}(μ-O)$_2$(dpaq^{2Me})$_2$]$^+$, [Mn^{III}(OOH)(dpaq^{2Me})]$^+$, and [Mn^{III}(O_2)(dpaq^{2Me})], with the product identity changing with the reaction acidity and amount of H_2O_2. The assignments of these species are supported by spectroscopic experiments and electronic structure calculations. We also explore the interconversion of these intermediates by the addition of acid or base and investigate the reactivity of the peroxomanganese complexes with substrates.

Experimental

Materials and Instrumentation. All chemicals were obtained from commercial vendors at ACS grade or better and were used without further purification unless otherwise noted. Diethyl ether was dried and degassed using a PureSolv solvent purification system. $[Mn^{II}(dpaq^{2Me})](OTf)$, and $[Mn^{III}(OH)dpaq^{2Me})](OTf)$ were prepared as reported previously.[74] Electronic absorption experiments were performed using either an Agilent 8453 spectrophotometer interfaced with an Unisoku cryostat or a Varian Cary 50 Bio UV-Visible spectrophotometer with a Quantum Northwest TC 1 temperature controller.

Reactions of $[Mn^{III}(OH)(dpaq^{2Me})]^+$ with H_2O_2 to give 2. A 1.25 mM solution of $[Mn^{III}(OH)(dpaq^{2Me})]^+$ (**1**) was prepared in MeCN and transferred to a quartz cuvette. Then, 10 equiv. of H_2O_2 were added to the cuvette via syringe while monitoring the reaction by electronic absorption spectroscopy at 25 °C. The resultant amber colored species **2** was further characterized by EPR, ^{1}H NMR, and XAS spectroscopies (vide infra). The thermal decay of **2** was also monitored using electronic absorption spectroscopy at 25 °C.

For reactivity studies with 2,4-ditertbutylphenol, a 1.25 mM solution of **2** was prepared in MeCN in a quartz cuvette. Upon full formation of **2**, an excess of 2,4-ditertbutylphenol, dissolved in 100 μL of MeCN, was added to the cuvette via syringe while monitoring the reaction by electronic absorption spectroscopy at 25 °C. The pseudo-first-order decay rate for this reaction (k_{obs}) was determined by fitting the change in absorbance at 700 nm as a function of time. When the reaction was complete, the organic products were collected after passing the solution through a silica plug and eluting with CH_2Cl_2. The solvent was removed, and the organic products were redissolved in MeCN-*d3* for analysis by ^{1}H NMR spectroscopy.

Reactions of 1 with H_2O_2 and $HClO_4$ to give 3. A 1.25 mM solution of **1** was prepared in MeCN and transferred to a quartz cuvette. 5 equiv. H_2O_2 and 0.1 equiv. $HClO_4$ were simultaneously added to the cuvette at -40 °C while monitoring the reaction by electronic absorption spectroscopy. This reaction resulted in the formation of a dark green species **3**, which was further characterized by electrospray ionization mass spectrometry (ESI-MS), and electronic absorption, EPR, and ^{1}H NMR spectroscopies. The thermal decay of **3** was monitored via electronic absorption spectroscopy at -40°C. The sensitivity of **3** to the presence of a base was determined by adding 2 equiv. triethylamine to a fully formed solution of **3** at -40°C.

For reactivity studies of **3** with thioanisole, a 1.25 mM solution of $[\mathrm{Mn^{III}(OH)(dpaq^{2Me})}]^+$ was prepared in MeCN and transferred to a quartz cuvette. 5 equiv. H_2O_2 and 0.1 equiv. $HClO_4$ were simultaneously added to the cuvette at -40 °C, while monitoring the reaction by electronic absorption spectroscopy. When **3** was fully formed, 10 equiv. thioanisole were added via syringe and the reaction was monitored via electronic absorption spectroscopy. When the reaction was complete, the solution was passed through a silica plug and the organic products were collected. The solvent was removed, and the organic products were redissolved in $CDCl_3$ and 1.0 equiv. (relative to Mn) benzoquinone was added. The products were analyzed by ^{1}H NMR spectroscopy.

Reactions of 1 with H_2O_2 and triethylamine to give 4. A 1.25 mM solution of **1** was prepared in MeCN and transferred to a quartz cuvette. 5 equiv. H_2O_2 and 2 equiv. triethylamine (Et_3N) were simultaneously added to the cuvette at 0 °C while monitoring the reaction by electronic absorption spectroscopy. The resultant bright green colored species, **4**, was further characterized by EPR and ^{1}H NMR methods (vide infra). The thermal decay of **4** was also monitored using electronic absorption spectroscopy at 0 °C. The acid sensitivity of **4** was assessed by titrating $HClO_4$ into a fully formed solution of **4** at 0 °C via syringe. Each 100 μL injection contained 1.0 equiv. $HClO_4$ and a total of 4.0 equiv. were added. The reaction was monitored by electronic absorption spectroscopy.

For kinetic studies of **4** with cyclohexane carboxaldehyde, a 1.25 mM solution of **4** was prepared at -40°C. After the complex had fully formed, a 100 μL aliquot of an MeCN solution containing an excess of cyclohexane carboxaldehyde (10 to 100 equiv.) was added, and the reaction was monitored via electronic absorption spectroscopy. The pseudo-first-order rate constant for the reaction of **4** with cyclohexane carboxaldehyde was determined by fitting the decay of the feature at 615 nm over time.

Acquisition of EPR Data. EPR experiments were performed on a Bruker EMXplus spectrometer with Oxford ESR900 continuous-flow liquid helium cryostat and Oxford ITC503 temperature system. EPR spectra of **2** and **3** were collected at 10 K (9.64 GHz microwave frequency, 2 mW microwave power, 0.4 mT modulation amplitude, 100 kHz modulation frequency). Spin quantification of the 16-line EPR signal of **2** was determined against a sample of $[Mn^{III}Mn^{IV}(\mu\text{-}O)_2(N4Py)_2]^+$ prepared by the addition of 5 equiv. H_2O_2 to a 10 mM solution of $[Mn^{II}(N4Py)(OTf)](OTf)$ in 2,2,2-trifluoroethanol.[63] For **4**, EPR spectra were collected at 10 K (9.64 GHz microwave frequency, 0.126 mW microwave power, 0.4 mT modulation amplitude, 100 kHz modulation frequency). Additionally, the spectrum of **4** was simulated and fit using EasySpin.[75]

Acquisition of ^{1}H NMR Data. ^{1}H NMR samples of **1, 3,** and **4** were prepared as described above from a 5 mM solution of **1** in d3-MeCN. Due to the instability of **3** and **4** at room temperature, ^{1}H-NMR data were collected at -40 °C on a Bruker DRX 500 MHz spectrometer with an acquisition time of 0.27 s and a D1 of 0 s with a spectral width of 150 to -100 ppm. At least 1000 scans were accumulated to provide sufficient signal-to-noise for each sample. Spectra were baseline-subtracted with the multipoint fitting procedure using spline functions as available in

MestReNova. ^{1}H NMR data were also collected for **2** at room temperature on a 400 MHz Bruker AVIIIHD NMR with the same acquisition parameters as the other complexes.

Acquisition and Analysis of X-Ray Absorption Data. A sample of **2** was prepared by adding 10 equiv. H_2O_2 to a 4 mM solution of **1** in MeCN at 25 °C while monitoring via electronic absorption spectroscopy. When **2** had fully formed, the solution was injected into a sample holder with a Kapton tape window and immediately frozen in liquid nitrogen. A sample of **3** was prepared in a similar fashion by treating a 5 mM solution of **1** with 5 equiv. H_2O_2 and 0.1 equiv. $HClO_4$ at -40°C. When **3** had fully formed, as confirmed by electronic absorption spectroscopy, the solution was injected into a sample holder and frozen in liquid nitrogen. The Mn K-edge XAS data were collected at Stanford Synchotron Radiation Lightsource (SSRL) on Beamline 7-3. Spectra were collected at 15 K over an energy range of 6300-7300 eV using a 30-element Ge array. Reference spectra for manganese foil were also collected with each scan and were calibrated by assigning the zero crossing of the second derivative of the foil K-edge energy to 6539.0 eV. The rising edge of the spectra were monitored for photoreduction during data collection but photoreduction was not observed.

The Athena program[76] was used for XAS data reduction and averaging. A background correction was applied by fitting the pre-edge background with a Gaussian function and subtracting this function from the whole spectrum. Then low-frequency background was removed by applying a spline correction. EXAFS fitting was performed on $k^3\chi(k)$ data using the Artemis program.[76] Phase and amplitude functions were obtained from FEFF as implemented in Artemis using a structural model of the related complex $[Mn^{III}Mn^{IV}(\mu\text{-}O)_2(dpaq)_2]^+$ from previously reported DFT calculations.[77] For each fit, the number of atoms in each shell (n) was held constant and the average distances between Mn and scattering atoms (r) and Debeye-Waller factors (σ^2) were optimized.

The threshold energy, E_0, was optimized in each fit, but was kept common for every shell of each fit. n was systematically varied between fits and the goodness-of-fit was determined using the R-factor:

$$R = \sum_{i=1}^{N} \left(\chi_i^{data} - \chi_i^{fit}\right)^2 / \sum_{i=1}^{N} \left(\chi_i^{data}\right)^2$$

The Mn K-edge pre-edge feature was fit using the Fityk program.[78] Three psuedo-Voigt line shapes with a fixed ratio of 1:1 Gaussian:Lorentzian functions and varied energy position, peak height, and full width at half maximum were used to fit the pre-edge area. The pseudo-Voigt function was also used to fit the background and rising edge contributions.

Electronic Structure Calculations. Density functional theory calculations were performed using ORCA 4.2.[79] Geometry optimizations and analytical frequency calculations used the TPSS functional[80] and the def2-TZVP basis set[81] for Mn, O, and N, with the def2-SVP basis set[82] for C and H. The calculations used the RI approximation[83] with the def2/J auxiliary basis set.[81] Single point calculations used the TPSSh functional[84-85] and def2-TZVPP basis set for all atoms. Solvation effects in acetonitrile were included using the CPCM SMD model in ORCA.[86] Electronic transition energies were determined using TD-DFT with the B3LYP functional[87] and the def2-TZVP basis set for Mn, O, and N, and def2-SVP for C and H. The auxiliary basis set def2-TZVP/C[88] and the RIJCOSX approximation[89-90] were used. Electronic structures were also explored using CASSCF calculations with NEVPT2 corrections.[91-93] The calculations used an active space of CAS(4, 5) to include only the $\mathrm{Mn^{III}}$ 3d orbitals and electrons, with the def2-TZVP basis set for Mn, O, and N, and the def2-SVP basis set for C and H. Auxillary basis sets def2/J and def2-SVP/C were used. The calculations included 50 singlet, 45 triplet, and 5 quintet roots.

Results and Discussion

Reaction of [Mn^{III}(OH)(dpaq^{2Me})](OTf) with H_2O_2. When 10 equiv. H_2O_2 are added to a solution of [Mn^{III}(OH)(dpaq^{2Me})]$^+$ (**1**) in MeCN at 25°C, **1** is rapidly converted to a new species **2** with intense features at 500 and 710 nm (ε = 1490 $M^{-1}cm^{-1}$ and 330 $M^{-1}cm^{-1}$, respectively) (Figure 1). This conversion proceeds through a short-lived intermediate with features at 610 and 770 nm, which forms 3 seconds after the addition of H_2O_2 (Figure 1, purple dashed traces) and persists for only 2 seconds (Figure 1, inset). At 25°C, **2** decays over a period of 24 hours to regenerate **1** in 99% yield, determined using the reported extinction coefficient for **1** (Figure 2).[74, 94] To further characterize **2**, EPR data were collected for a frozen MeCN solution. The resultant EPR spectrum has a 16-line signal with g = 2.01 and A = 7.70 mT (Figure 3). Spin quantification reveals that this signal accounts for roughly 80% of the total manganese in this sample. The EPR and electronic absorption spectra of **2** are similar to those previously reported for bis(μ-oxo)dimanganese(III,IV) complexes (Table S1), providing strong evidence for the assignment of **2** as [Mn^{III}Mn^{IV}(μ-O)$_2$(dpaq^{2Me})$_2$]$^+$ (Scheme 1).[63, 77, 95-98]

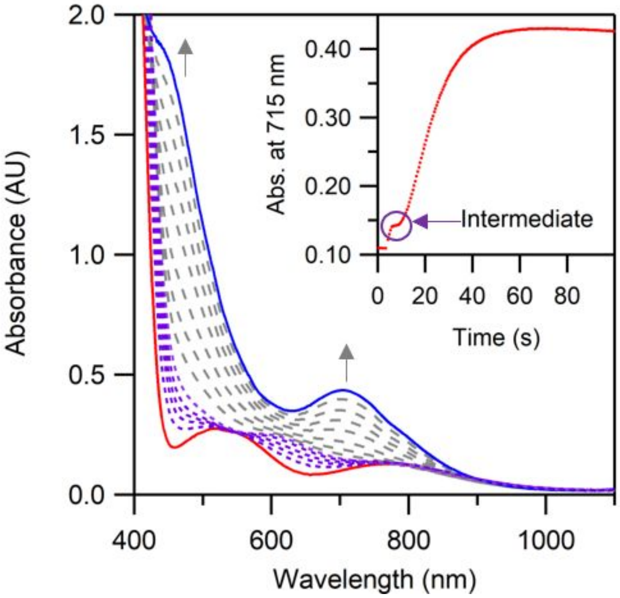

Figure 1. Electronic absorption spectra following the reaction of a 1.25 mM solution of [Mn^{III}(OH)(dpaq^{2Me})]$^+$ (**1**) in MeCN at 25 °C (red trace) with 10 equiv. H_2O_2 to form **2** (blue trace).

Inset: Time course of the formation of the feature at 710 nm. The formation of **2** is preceded by the formation of a fleeting intermediate (highlighted using the purple dashed traces) which forms within 3 seconds and persists for ~2 seconds before the formation of **2**.

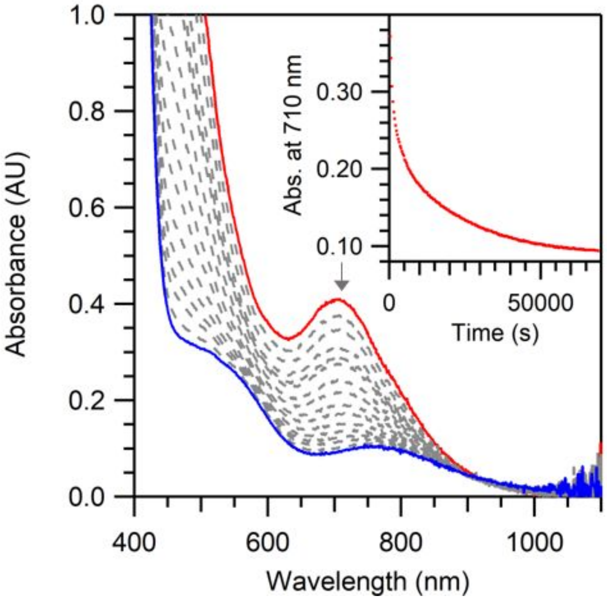

Figure 2. Electronic absorption spectra monitoring the thermal decay of a 1.25 mM solution of **2** (red trace) in MeCN at 25°C to regenerate [Mn^{III}(OH)(dpaq^{2Me})]$^+$ (**1**; blue trace). Inset: Time course of the decay of the feature at 710 nm.

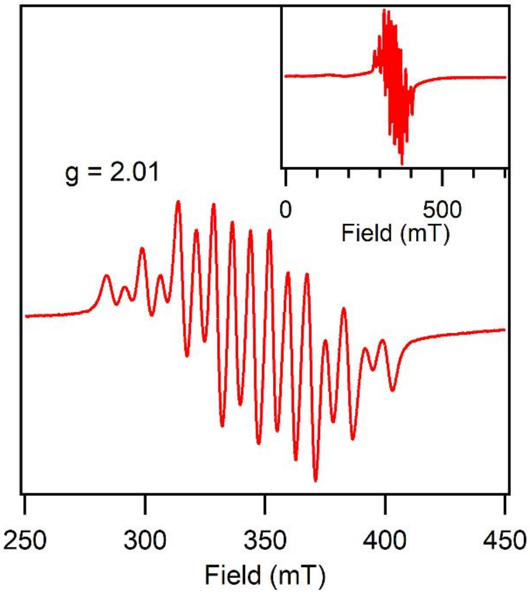

Figure 3. 10 K perpendicular-mode EPR spectrum obtained following the reaction of a 3 mM solution of [Mn^{III}(OH)(dpaq^{2Me})]$^+$ (**1**) with 1 equiv. of H_2O_2 in MeCN at 25 °C to form **2**. The 16-line signal is consistent with a bis(μ-oxo)dimanganese(III,IV) complex, which accounts for roughly 80% of total Mn in the sample. Inset: Full range of the collected spectrum.

Scheme 1. Balanced reaction showing the formation of a bis(*m*-oxo)dimanganese(III,IV) complex from the reaction of a Mn^{III}-hydroxo complex and H_2O_2.

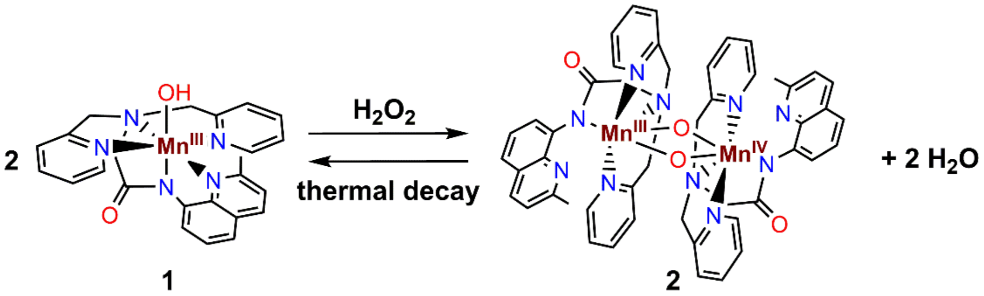

The assignment of **2** as a bis(μ-oxo)dimanganese(III,IV) complex is further supported by Mn K-edge XAS data. The X-ray absorption near edge structure (XANES) of **2** (Figure 4) is similar to that of the parent complex **1**. In particular, the Mn K-edge energy of **2** (6550.2 eV) is within 0.2 eV of **1** and is comparable to edge energies of other bis(μ-oxo)dimanganese(III,IV) species (Table S1).[77, 95] The XANES spectrum of **2** shows a pre-edge peak at 6540.9 eV. The pre-edge area was found to be 19.4, which is larger than that reported for monomeric manganese complexes supported by this ligand (~4; see Table S1). However, this large area is consistent with those of bis(μ-oxo)dimanganese(III,IV) complexes (22.9 and 19.6; see Table S1).[95]

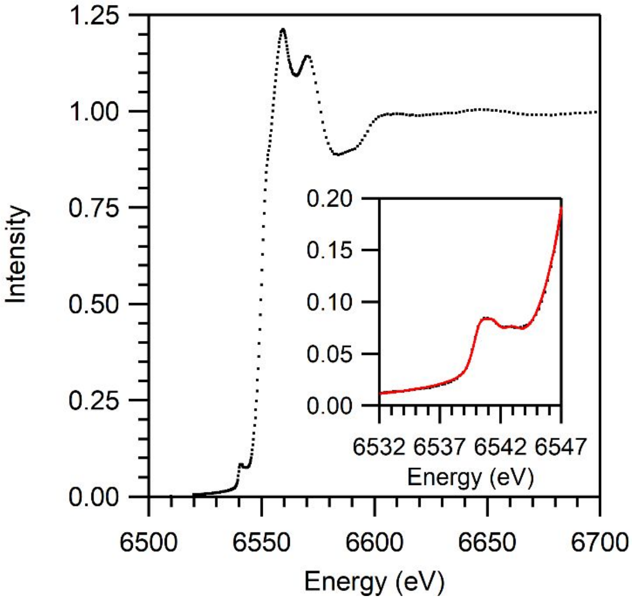

Figure 4. Mn K-edge XANES spectrum for **2**. Inset: Pre-edge feature of **2**. Experimental data are shown in black and fits are shown in red.

The Fourier transform EXAFS spectrum of **2** features two large peaks at 1.32 and 2.45 Å with shoulders at 1.66 and 2.88 Å (Figure 5). These data are best fit with shells of two O atoms at 1.81 Å, 4 N atoms at 2.08 Å, 8 C atoms at 2.91 Å, and a single Mn at 2.65 Å (Table 1). These distances are in excellent agreement with EXAFS analyses for other bis(μ-oxo)dimanganese(III,IV) complexes,[95] which showed Mn-O and Mn-Mn distances of 1.82 and 2.63 Å, respectively.

The observation that **1** reacts with H_2O_2 to generate a bis(μ-oxo)dimanganese(III, IV) complex is similar to that observed for the related complex $[Mn^{III}(OH)(dpaq)]^+$.[77] The bis(μ-oxo)dimanganese(III,IV) species generated from $[Mn^{III}(OH)(dpaq)]^+$ showed poorly resolved UV-vis features at 540 and 660 nm and decayed to regenerate the parent Mn^{III}-hydroxo complex (Figure S1).[77] The structural parameters of **2** are in good agreement with the DFT structure of $[Mn^{III}Mn^{IV}(\mu\text{-}O)_2(dpaq)_2]^+$ reported previously; however, the EXAFS-derived Mn-Mn distance of **2** is shorter than that in the DFT structure (2.65 vs 2.79 Å, respectively). The discrepancy between the calculated Mn-Mn distance and that observed by EXAFS could be due to the use of a double-zeta basis set and/ or the lack of dispersion interactions in determining the DFT structure.[77]

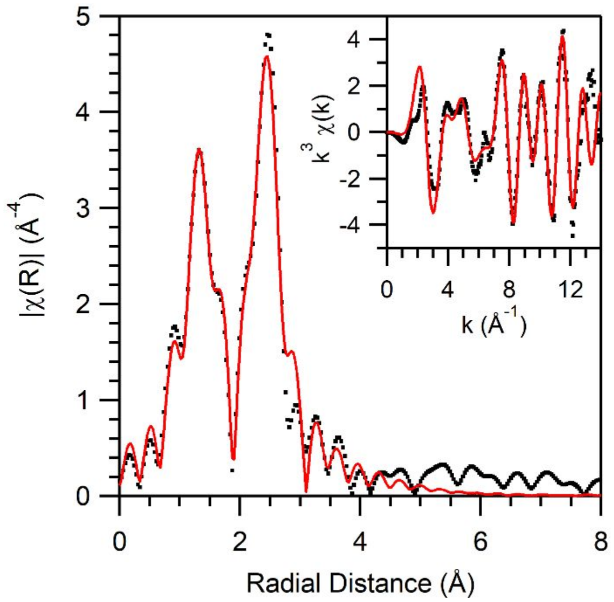

Figure 5. Fourier transform of Mn K-edge EXAFS data for **2** in frozen MeCN. Inset: EXAFS spectrum for **2**. Experimental data are shown in black and fits are shown in red.

Table 1. EXAFS Fit Parameters for **2**

	Mn-Mn			***Mn-N***			***Mn-O***			***Mn-C***			
fit	***n***	***r (Å)***	***σ²***	***n***	***r (Å)***	***σ²***	***n***	***r (Å)***	***σ²***	***n***	***r (Å)***	***σ²***	***goodness of fit***[a]
1	1	1.94	0.005										0.583
2	1	2.56	0.004	6	1.78	0.014							0.530
3	1	3.65	0.007	4	1.76	0.008							0.475
4	1	2.71	0.002	4	1.55	0.027	2	1.86	0.009				0.223
5				5	2.00	0.017	2	1.88	0.005	6	2.87	0.001	0.472
6	**1**	**2.65**	**0.003**	**4**	**2.08**	**0.014**	**2**	**1.81**	**0.005**	**8**	**2.91**	**0.006**	**0.058**

[a]Evaluated using the R-factor

Previous studies of bis(μ-oxo)dimanganese(III, IV) complexes reveal phenol oxidation as a common model of reactivity.[63, 77, 95-96, 98] Reactions of **2** with 100 equiv. 2,4-di-*tert*-butylphenol result in the decay of the feature at 710 nm over 300 s at 25 °C (Figure S2, top). An analysis of the resulting solution by ^{1}H NMR spectroscopy reveals the formation of 3,3',5,5'-*tetra*-*tert*-butylbiphenyl-2,2'-diol (Figure S3). This biphenol is a characteristic product when 2,4-di-*tert*-butylphenol has donated a hydrogen atom to an oxidant. Thus, the reactivity of **2** further supports its formulation as a bis(μ-oxo)dimanganese(III, IV) complex.[63, 77, 95-96, 98]

Reaction of [Mn^{III}(OH)(dpaq^{2Me})](OTf) with H_2O_2 in the presence of an acid. In the reaction of **1** with H_2O_2 at 25 °C, there is evidence of a short-lived intermediate with absorption features at 610 and 800 nm that precedes the formation of the bis(μ-oxo)dimanganese(III, IV) complex **2** (Figure 1). The previous study of the reaction of [Mn^{III}(OH)(dpaq)]$^+$ with H_2O_2 reported formation of a similar bis(μ-oxo)dimanganese(III, IV) complex, but in that case no intermediates were observed.[77] In an effort to characterize this fleeting intermediate, we explored the reaction of **1** with H_2O_2 in the presence of an acid at the substantially lower temperature of -40 °C. Through exploratory experiments in which we varied the amount of acid, we observed that this fleeting intermediate (**3**) was most stable when 5 equiv. H_2O_2 and 0.1 equiv. $HClO_4$ were added simultaneously to a solution of **1** in MeCN at -40 °C. In this reaction, the purple Mn^{III}-hydroxo complex is rapidly converted to a dark green species **3** with absorption features at 610 and 770 nm (ε = 210 and 105 $M^{-1}cm^{-1}$, respectively; see Figure 6, top). The absorption maxima of **3** occur at the same energy as that of the short-lived intermediate briefly observed during the formation of **2**, though they are much better resolved in the presence of acid (Figure S4). Importantly, the formation of **3** from **1** under these conditions proceeds with isosbestic behavior. The decay profile of **3** (Figure 6, bottom inset) is complex. In the first 1200 seconds, **3** decays relatively slowly, losing 5% of its absorption intensity at 610 nm. After 1200 seconds, the absorption intensity drops much more rapidly (losing 11% of its intensity at 610 nm in 360 seconds). After roughly 1560 seconds, the absorption intensity rises again, revealing the formation of the bis(μ-oxo)dimanganese(III,IV) complex **2**. From this profile, we propose that the self-decay of **3** involves the slow accumulation of an intermediate within the first 1200 seconds. As this intermediate accumulates, it increases the decay rate of **3**, leading to the more rapid decay phase that eventually yields the bis(μ-oxo)dimanganese(III,IV) product.

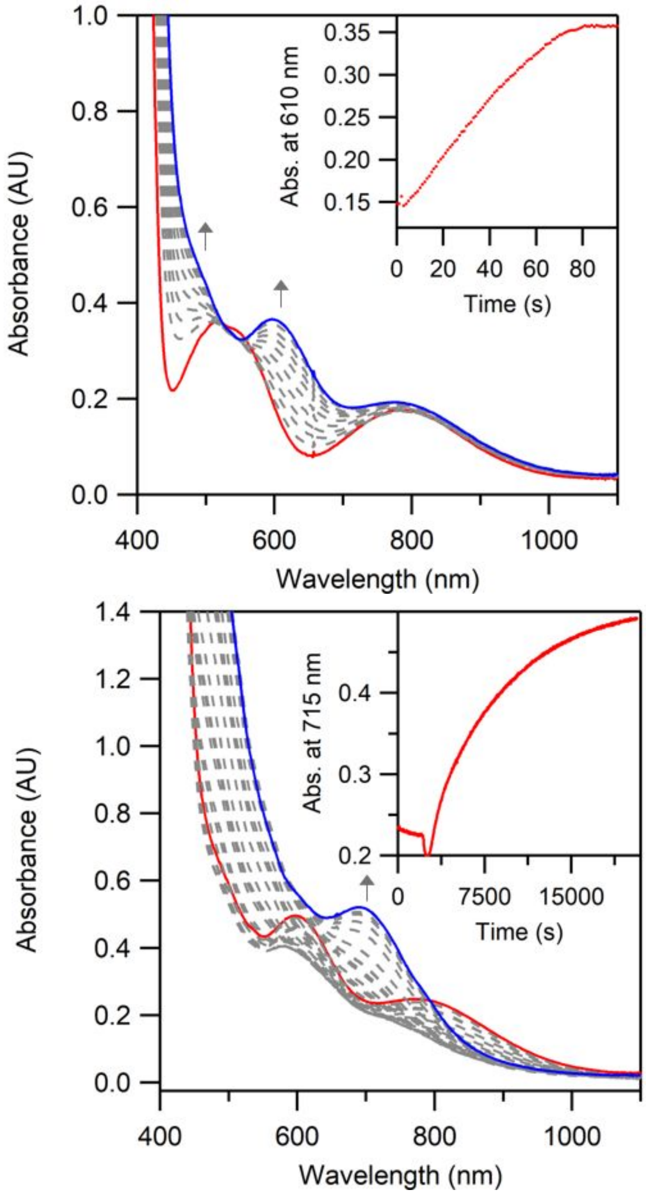

Figure 6. Top: Electronic absorption spectra for the reaction of a 1.25 mM solution of **1** (red trace) with 5 equiv. H_2O_2 and 0.1 equiv. $HClO_4$ to form **3** (blue trace) at -40°C. Inset: Time course for the growth of the feature at 610 nm. Bottom: Electronic absorption spectra for the decay of **3** at -40°C. The decay product (blue trace) is the bis(μ-oxo)dimanganese(III,IV) complex **2**. Inset: Time course of the self-decay reaction. **3** is stable for ~1200s before a rapid decay process initiates the formation of **2**.

While 0.1 equiv. $HClO_4$ was found to best stabilize **3**, other formation conditions were attempted. Complex **3** can also be generated using 5 equiv. H_2O_2 and 1 equiv. $HClO_4$; however, under these conditions **3** begins to decay almost immediately even at -40°C (Figure S5).

Interestingly, the decay pathway for **3** is sensitive to the amount of acid. When **3** is generated using 1 equiv. $HClO_4$, the decay product shows a nearly featureless UV-vis spectrum, consistent with the formation of a Mn^{II} product (Figure S5, bottom). Thus, the increase in acid concentration appears to prevent the conversion of **3** to **2**. We also attempted to form **3** using 5 equiv. H_2O_2 and 1 equiv. of acetic acid. While **3** does form under these conditions, the feature at 610 nm is not as well resolved as in other reactions (Figure S6, top). Moreover, when **3** is formed using acetic acid, **3** begins to decay rapidly after ~20 seconds even at -40 °C (Figure S6, bottom). Based on these results, we used 5 equiv. H_2O_2 and 0.1 equiv. $HClO_4$ for characterization and reactivity studies.

The influence of acid strength and concentration on the formation and stability of **3** suggests that this species might be a Mn^{III}-hydroperoxo complex (Scheme 2). To date, only four Mn^{III}-hydroperoxo species supported by non-porphyrin ligands have been reported.[66-67, 69] Two of these species, $[Mn^{III}(OOH)(14\text{-}TMC)]^{2+}$ [67] and $[Mn^{III}(OOH)(13\text{-}TMC)]^{2+}$,[66] were generated by protonation of the corresponding side-on peroxomanganese(III) complexes by a strong acid. The $[Mn^{III}(OOH)(BDPP)]$ and $[Mn^{III}(OOH)(BDP^{Br}P)]$ complexes were formed via a HAT reaction between TEMPOH and the Mn^{III}-superoxo complexes.[69] These reports differ from our method for generating **3**, which involves direct reaction of a Mn^{III}-hydroxo species (**1**) with H_2O_2. Indeed, the conversion of **1** to **3** by the addition of 5 equiv. H_2O_2 and 0.1 equiv. $HClO_4$ shows isosbestic points at 510 and 560 nm (Figure 6, top), suggesting a direct conversion from **1** to **3**. Precedent for the formation of a metal-hydroperoxo adduct from a metal-hydroxo species comes from iron chemistry.[99] The formation of Fe^{III}-hydroperoxo species from an Fe^{III}-hydroxo adduct has been proposed to proceed through an initial protonation of the hydroxo moiety from H_2O_2 to produce the Fe^{III}-aqua species and the hydroperoxyl anion (Scheme 3, top pathway).[99] The formation of the Fe^{III}-hydroperoxo species then follows from a ligand exchange of water for the hydroperoxyl anion. In the formation of a Fe^{III}-OOH complex reported by Xu and coworkers, this process was shown to be assisted by the presence of a weak acid in solution, which also results in the formation of the Fe^{III}-aqua species and aids in the formation of the Fe^{III}-hydroperoxo species (Scheme 3, bottom pathway).[100] That study reported that strong acids could protonate the distal oxygen of the hydroperoxo moiety, promoting heterolytic O-O bond cleavage resulting in an Fe^{V}=O species and water.[100] The dependence of the stability of **3** on the amount of acid present in solution supports a ligand substitution mechanism, where the hydroxo ligand in **1** is replaced by H_2O_2, yielding the Mn^{III}-hydroperoxo complex **3** and water (Scheme 2).

Scheme 2. Summary of the reactions of a Mn^{III}-hydroxo complex with H_2O_2 in the absence and presence of strong acid. The reactions are not balanced but indicate the Mn complexes detected by spectroscopic methods.

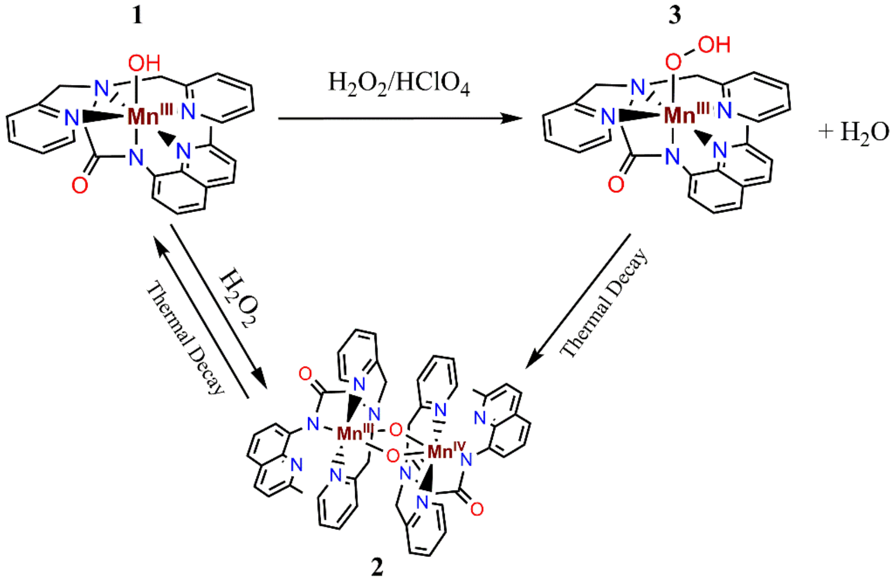

Scheme 3. Potential pathways for the formation of a metal(III)-hydroperoxo complex from the reaction of a metal(III)-hydroxo species with H_2O_2 in the presence of acid.

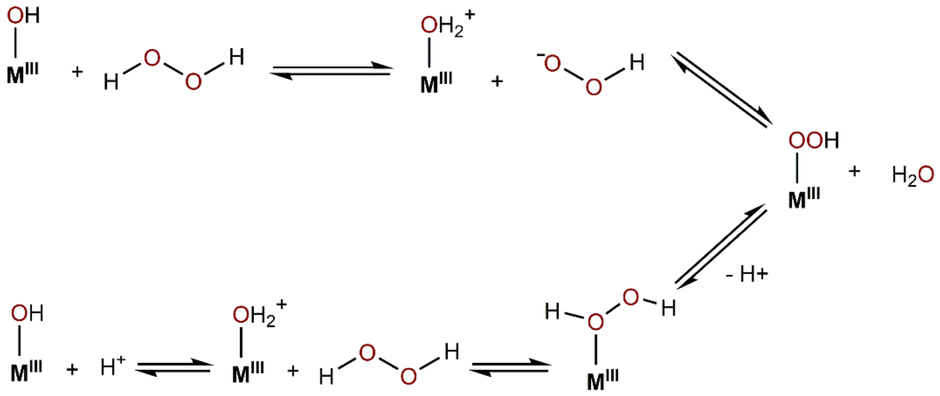

To further assess our proposal that **3** is a Mn^{III}-hydroperoxo species, as well as evaluate the proposed ligand exchange mechanism, we determined the amount of hydrogen peroxide required to result in the maximum formation of **3**. The complex **3** can be formed in high yields by adding as few as 2 equiv. H_2O_2 to **1** (Figure S7, top). We observed no change in the lifetime of **3** when this complex was generated using either 2 or 5 equiv. H_2O_2. When **1** is treated with only 1 equiv. H_2O_2, the resultant spectrum can be reproduced using a linear combination of the absorption spectra of **1** and **3** with a **1**:**3** ratio of 0.46:0.54 (Figure S7, bottom). This result supports our proposal of an exchange equilibrium between the Mn^{III}-hydroxo complex and the putative Mn^{III}-hydroperoxo complex.

Complex **3** was further characterized by EPR, ^{1}H NMR, Mn K-edge X-ray absorption spectroscopies, and ESI-MS. The perpendicular-mode EPR spectrum of a frozen solution of **3** shows a feature near g = 2.0 with a six-line hyperfine splitting pattern (Figure S8). This feature is consistent with the presence of a Mn^{II} species, but accounts for only 3% of the manganese in solution. The parallel-mode EPR spectrum of **3** only shows a weak feature due to O_2 (Figure S8). Thus, the majority of Mn in **3** is in an EPR-silent form. On this basis, **3** contains spin-coupled multinuclear Mn centers and/ or mononuclear Mn^{III} centers with large zero-field splitting. Notably, the mononuclear Mn^{III}-hydroxo complex **1** is also EPR silent.[94]

Due to the instability of **3** at room temperature, ^{1}H-NMR experiments were performed at -40 °C. The ^{1}H NMR spectrum of **3** is similar to, but distinct from, that of **1** (Figure 7 and Table 2). The upfield region of the ^{1}H NMR spectrum of **3** shows 4 peaks at -13, -20, -34, and -44 ppm, which are at essentially identical positions to peaks observed for **1** (Table 2). The resonances in this region arise from quinoline protons, and the similarities between **1** and **3** require similar Mn^{III}-quinoline interactions.[101] The downfield region of the ^{1}H NMR spectrum of **3** shows slight variations compared to **1**. The broad features at 91.55 ppm and 50.97 ppm in **1**, previously assigned as pyridine protons,[101] shift by nearly 10 ppm to 102.09 ppm and 62.91 ppm, respectively. We considered the possibility that these minor peak shifts were due to the presence of water in the solution, as observed previously for similar complexes.[102] However, the addition of water or acid in the absence of H_2O_2 did not result in the peak shifts observed here (Figure S9). Overall, the ^{1}H NMR data are consistent with the dpaq^{2Me} ligand of **3** being in an environment nearly identical to that of **1**, which would be expected for a Mn^{III}-OOH species.

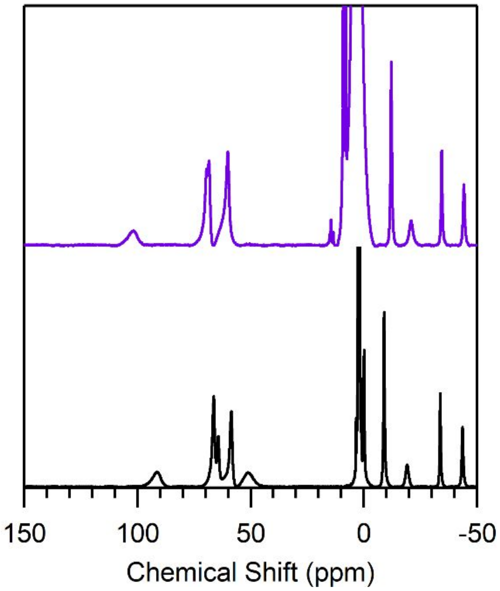

Figure 7. Low temperature ^{1}H NMR spectra of 3 mM **1** (black trace) in *d3*-MeCN and a 3 mM solution of **3** formed with 5 equiv. H_2O_2 and 0.1 equiv. $HClO_4$ (purple trace) in *d3*-MeCN. A larger version of this spectrum is available in Figure S9.

Table 2. ^{1}H NMR Chemical Shifts for **1**, **3**, and **4** in *d3*-MeCN at -40°C.

Assignments	**1**	**3**	**4**
1	ppm	ppm	ppm
H(py)	91.55	102.09	91.05
H(qn)	67.31	69.89	44.50
H(qn)	64.57	68.75	31.52
H(qn)	58.49	60.09	16.70
H(py)	50.97	62.91 (sh)	11.59
H(py)	-9.00	-12.78	11.18
H(qn)	-20.09	-20.80	-6.48
H(qn)	-33.87	-34.33	-17.24
H(qn)	-43.72	-44.11	-37.17

The XANES region of **3** is remarkably similar to that of **1** (Table S1). The edge energy of **3** is 6550.5 eV, which is only 0.5 eV higher than that of **1** (Figure 8 and Table S1). Additionally, the pre-edge energy of **3** (6540.3 eV) is identical, within error, to that of **1**, while the pre-edge area of 6.3 is slightly larger (Table S1). The Fourier transform of the EXAFS region of **3** features a large peak at 1.77 Å with two smaller peaks at 2.24 and 2.54 Å (Figure 9). These data are well fit with a shell of two O/N atoms at 1.91 Å, 4 N atoms at 2.16 Å, and 5 C atoms at 2.92 Å (Table 3). This Mn-O bond length is in good agreement with that of **1**, which featured an O/N scattering shell at 1.89 Å, and with a related Mn^{III}-alkylperoxo complex that also had a scattering shell at 1.89 Å.[73, 103] The second shell at 2.16 Å is attributed to the equatorial nitrogen ligands and is in excellent agreement with values reported for **1** (2.17 Å), suggesting little change to the ligand binding at the Mn center. In total, the EPR, ^{1}H NMR, and XAS data for **3** are fully consistent with the assignment as a mononuclear Mn(III) species with a ligand environment very similar to that of **1**.

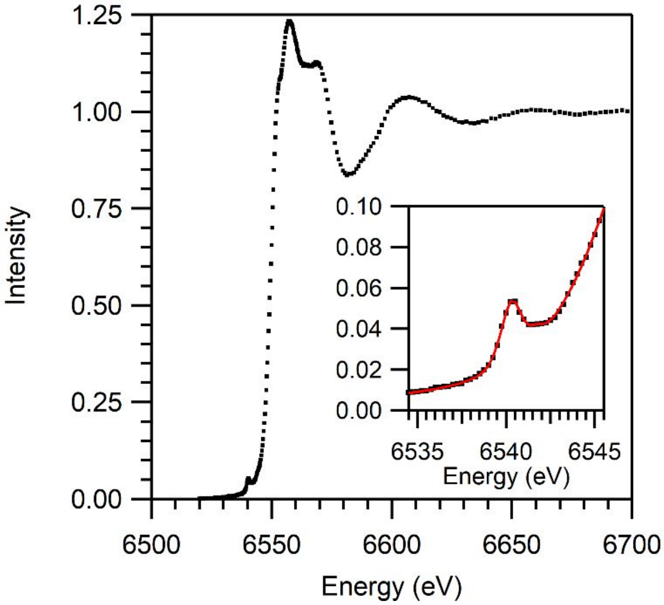

Figure 8. Mn K-edge XANES spectrum for **3**. Inset: Pre-edge feature of **3**. Experimental data are shown in black and fits are shown in red.

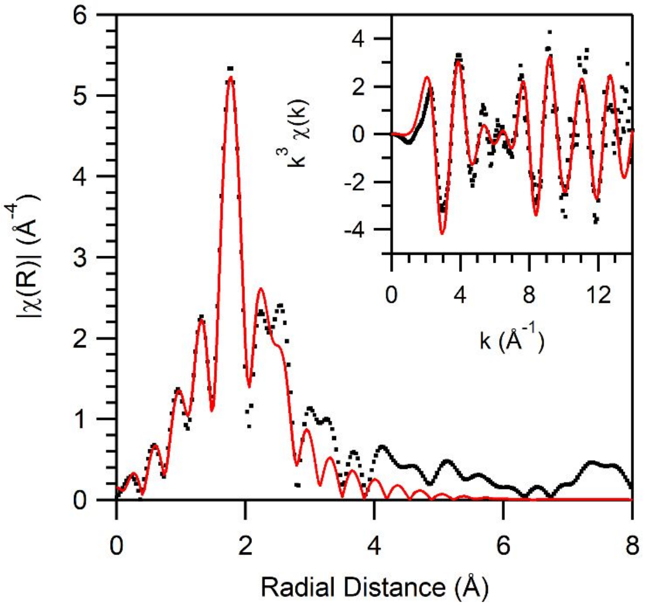

Figure 9. Fourier transform of Mn K-edge EXAFS data for **3** in frozen MeCN. Inset: EXAFS spectrum for **2**. Experimental data are shown in black and fit 4 (Table 3) is shown in red.

Table 3. EXAFS Fit Parameters for **3**

	Mn-O/N$_{axial}$			***Mn-O/N$_{equatorial}$***			***Mn-C***			
fit	***n***	***r (Å)***	***σ^2***	***n***	***r (Å)***	***σ^2***	***n***	***r (Å)***	***σ^2***	***goodness of fit[a]***
1	6	2.22	0.012							0.663
2	2	1.91	0.003	4	2.15	0.004				0.251
3	2	1.90	0.003	5	2.15	0.006				0.244
4	**2**	**1.91**	**0.003**	**4**	**2.16**	**0.004**	**5**	**2.92**	**0.006**	**0.122**
5	2	1.90	0.003	5	2.16	0.006	5	2.92	0.006	0.118

[a]Evaluated using the R-factor

ESI-MS measurements of **3** reveal a feature at *m/z* = 484.1, which is consistent with a Mn^{III}-OOH species (calc. *m/z* = 484.1; Figure S7). The remaining features in the spectrum are the result of the rapid decay of this complex under the experimental conditions. These features can be assigned as Mn^{III}-hydroxo species (calc. *m/z* = 468.1), the dpaq^{2Me}H$_2^+$ ligand (calc. *m/z* = 398.2), Na$^+$dpaq^{2Me}H (calc. *m/z* = 420.1), and [Mn^{II}(dpaq^{2Me})]$^+$ (*m/z* = 451.1).

Reaction of [Mn^{III}(OH)(dpaq^{2Me})](OTf) with H$_2$O$_2$ in the presence of base. Previous reports have indicated that end on Mn^{III}-hydroperoxo species and the corresponding Mn^{III}-peroxo species can be interconverted by the addition of base or acid, respectively.[66-67] We used a similar approach to assess our assignment of **3** as a Mn^{III}-hydroperoxo species. The reaction of the putative Mn^{III}-hydroperoxo complex **3** with triethylamine results in the rapid formation of a new bright green intermediate **4** with features at 450 and 615 nm (Figure 10). The electronic absorption spectrum of this complex is nearly identical to that of the Mn^{III}-peroxo complex supported by the unmodified dpaq ligand ([Mn^{III}(O$_2$)(dpaq)]$^+$).[104]

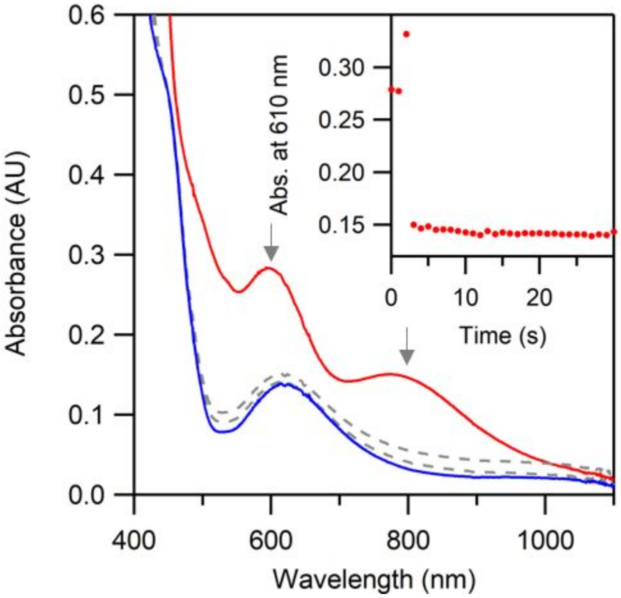

Figure 10. Electronic absorption spectrum of **3** generated using 5 equiv. H_2O_2 and 0.1 equiv. $HClO_4$ (red trace). The spectral changes (dashed gray traces) mark the reaction of **3** with 2 equiv. Et_3N to give the final product **4** (blue trace).

The new species **4** can also be generated from the reaction of **1** with H_2O_2 in the presence of triethylamine (Figure 11). In these reactions 5 equiv. H_2O_2 and 2 equiv. Et_3N were added to a 1.25 mM solution of **1** at 25°C. This reaction resulted in a spectrum identical to that of **4**, with features at 450 and 615 nm (ε = 442 and 108 $M^{-1}cm^{-1}$, respectively). In the case of **4** formed from the deprotonation of **3**, the intensity suggests only ~50% formation (Figure S11). At 25 °C, **4** quickly decays to a species with a spectral feature at 715 nm, consistent with formation of the bis(μ-oxo)dimanganese(III, IV) complex **2** as the decay product (Figure S12, top, and Scheme 4). Under these conditions **2** itself decays to give an 89% yield of the starting complex **1** over the course of 3 hours (Figure S12, bottom, and Scheme 4). Due to the instability of **4** at room temperature, further characterization and reactivity studies with this complex were performed at 0 °C. The electronic absorption signals of **4** are similar to those of side-on Mn^{III}-peroxo complexes (Table 4).[54-55, 57-58, 61, 63]

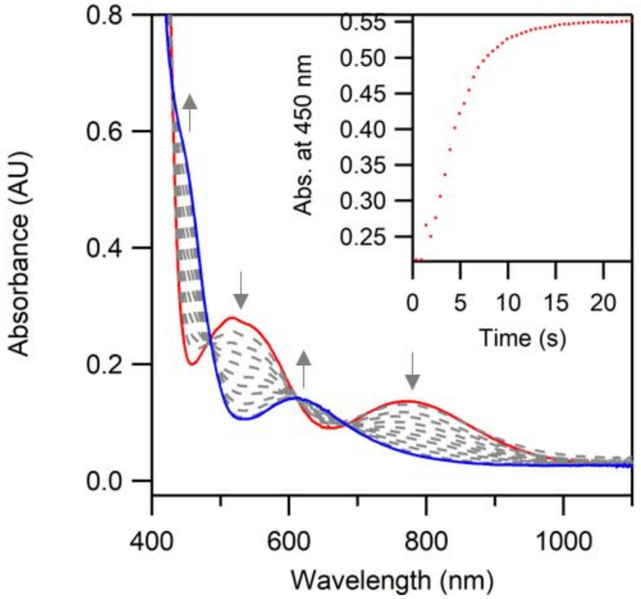

Figure 11. The reaction of a 3 mM MeCN solution of **1** with 5 equiv. H_2O_2 and 2 equiv. Et_3N at 25 °C results in the formation of **4** (blue trace). Inset: Time trace for the formation of the feature at 450 nm.

Scheme 4. Summary of the reactions of a Mn^{III}-hydroxo complex with H_2O_2 in the absence and presence of base. The reactions are not balanced but indicate the Mn complexes detected by spectroscopic methods.

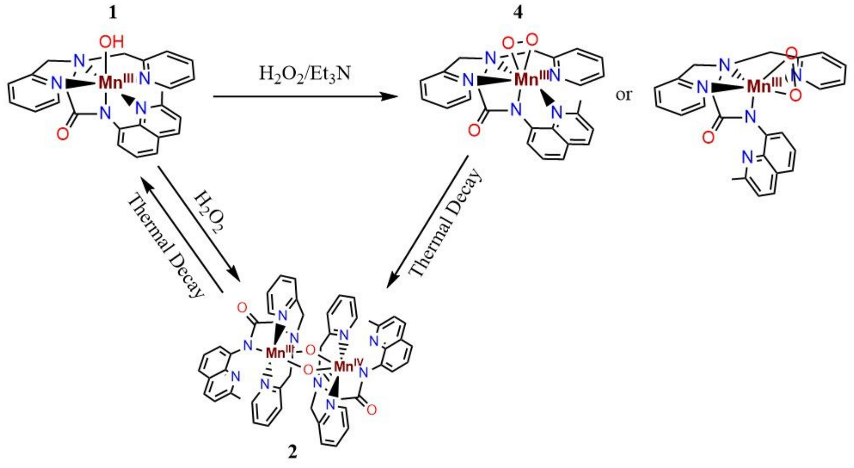

The interconversion of **3** to **4** by the addition of base provides further evidence to support the assignments of **3** and **4** as Mn^{III}-OOH and Mn^{III}-O_2 species, respectively. We also attempted the reverse reaction by adding $HClO_4$ to **4**. However, this reaction did not result in the formation of **3**. The inability to form **3** from the reaction of **4** with acid could point to significant structural distortion in **4** that renders it incapable of regenerating **3**. Alternatively, **3** is quite sensitive to the presence of acid in solution and it is possible that the complex cannot be detected under these conditions. It should be noted that the conversion of Mn^{III}-peroxo species to corresponding Mn^{III}-hydroperoxo species is quite rare, with only two known examples.[66-67]

The EPR spectrum of **4** at 10 K reveals an intense, broad derivative-shaped signal with an apparent *g* value of 8.6 (Figure 12). This unusual EPR spectrum can be nicely simulated for an S = 2 system with $g = 2.03$, $|D| = 2.41$ cm^{-1}, and $E/D = 0.20$ (Figure 12, red). This fit is insensitive to the sign of *D*. Several Mn^{III}-peroxo species show parallel-mode EPR signals around 80 mT; however, in most cases the signals display a six-line hyperfine splitting pattern that is absent in the EPR spectrum of **4** (Table 4).[54-55, 58, 61] For example, a broad, derivative signal spanning 50 – 120 mT was reported by Borovik and coworkers for an $S = 2$ Mn^{III}-peroxo species with $D = -2.0$ cm^{-1} and $E/D = 0.13$ although that signal had resolved hyperfine splitting from the ^{55}Mn center (A = 5.7 mT).[61] Low-field, derivative signals were also reported for trimanganese clusters by Agapie and coworkers.[105] For those systems, the signal was centered around 40-50 mT, which would correspond to a much higher apparent g value than we observe in **4**. These trimanganese species also showed additional features at higher field and thus are distinct from the EPR spectrum of **4**.[105]

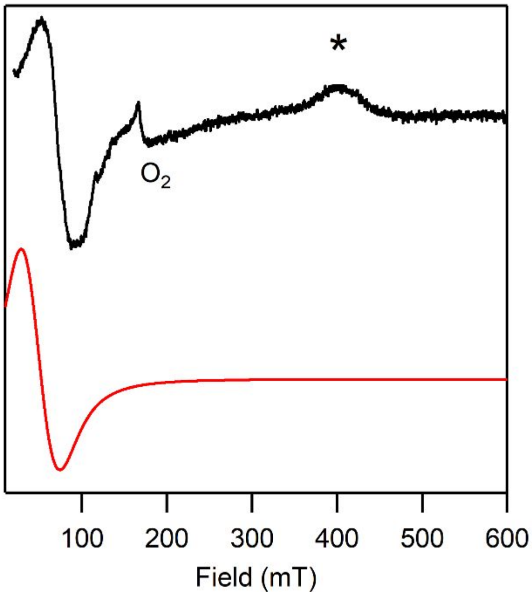

Figure 12. The parallel-mode EPR spectrum obtained at 10 K following the reaction of a 3 mM solution of $[Mn^{III}(OH)(dpaq^{2Me})]^+$ in 1:1 MeCN:toluene with 5 equiv. of H_2O_2 and 2 equiv. Et_3N at -40 °C (black) and the simulated spectrum (red). The intensity of the signal at 400 mT (*) varied greatly between sample preparations. On this basis, we tentatively attribute this signal to an unknown contaminant.

Table 4. Comparison of Spectroscopic Characteristics of Select Mn^{III}-peroxo Species.

Complex	***λ (nm)***	***g_{eff}***	***A***	***Reference***
4	450, 615	8.6	--	*This work.*
$[Mn^{III}(O_2)(Me_2EBC)]_+$	400, 650	7.96	6.84	58
$[Mn^{III}(O_2)(N4Py)]^+$	617	7.85	6.8	54, 63
$[Mn^{III}(O_2)(mL_5{}^2)]^+$	585	8.1	6.6	54
$[Mn^{III}(O_2)(Tp^{Ph2})(THF)]$	379, 435	8.3	9.1	55
$[Mn^{III}(O_2)(Pro_3Py)]^+$	580	8.3	--	57
$[Mn^{III}(O_2)(H_2bupa)]^-$	490, 660	8.2	5.7	61

Further insight into the solution structure of **4** was obtained by ^1H NMR experiments at -40 °C (Figure 13). The hyperfine shifted signals in the NMR spectrum of **4** are consistent with a mononuclear Mn^{III} species. While formal assignments of NMR resonances of **4** have not been made, there are two key features of this NMR spectrum that provide insight into its structure. First, the ^1H NMR spectrum for **4** has the same number of hyperfine shifted resonances as **1** (Figure 13 and Table 1). On this basis, the binding of the $dpaq^{2Me}$ ligand in **4** must have similarities to that of **1**. In particular, the pyridine groups in **4** must be symmetric, as a loss of symmetry would increase the number of hyperfine shifted resonances. Second, the resonances of **4** are contracted toward the 10 – 0 ppm region relative to **1**. This contraction could be attributed to a different factors. In the simplest case, this contraction could be caused by structural distortions required for a seven-coordinate Mn center with a side-on peroxo ligand. This distortion would include elongation of equatorial Mn-N bonds, increasing the distance between protons and the paramagnetic Mn center. Alternatively, the contraction could arise from large shifts in resonances of quinoline protons due to quinoline dissociation. We have previously assigned many of the upfield shifted peaks of a similar complex as quinoline resonances.[101] In the case of quinoline dissociation, these features would shift substantially downfield and potentially into the 10 – 0 pmm region. Quinoline would not alter the symmetry of the pyridine protons, consistent with the experimental spectrum.

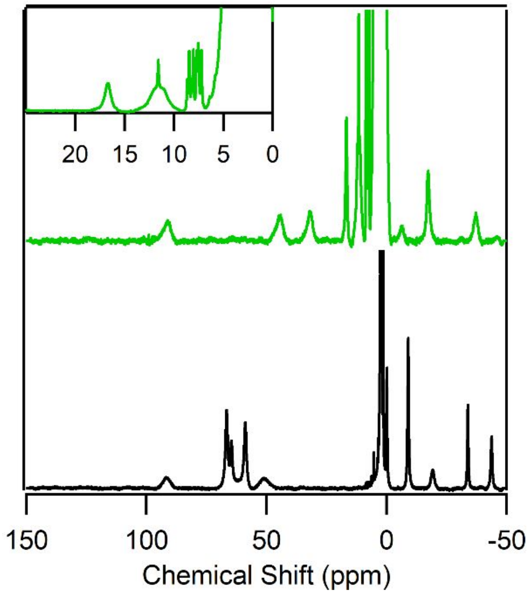

Figure 13. Low temperature ^{1}H NMR spectra of 3 mM **1** (black trace) in *d3*-MeCN and a 3 mM solution of **4** formed with 10 equivalents each of H_2O_2 and Et_3N (green trace) in *d3*-MeCN. Spectra were collected at -40°C. Inset: expanded view of the 25 to 0 ppm region showing overlapped features near 11 ppm. Peaks in the 9 to 7 ppm region correspond to free ligand. A larger version of this spectrum is available in Figure S9.

Electronic Structure Calculations. A) DFT Calculations for 1 and 3. To further understand the spectroscopic differences between **1** and **3**, and to more fully evaluate our assignment of **3** as a Mn^{III}-hydroperoxo adduct, we performed DFT calculations for these species. The optimized geometries and key structural parameters are shown in Figure 14. These structures indicate an elongation of the equatorial Mn^{III}-N bonds (Mn^{III}-N$_{eq}$) for **3** relative to **1** (2.22 vs 2.17 Å, respectively) as well as elongation of the Mn^{III}-O bond in **3** (1.86 vs 1.82 Å in **1**). The amide bond distance remains the same in both structures. The elongation of the Mn-O bond in **3** is reflected in the EXAFS analysis (1.91 vs 1.89 Å in **1**) however the EXAFS data indicate similar Mn^{III}-N$_{eq}$

bond lengths between **1** and **3** (2.17 and 2.16 Å, respectively). These structural changes are similar to those reported in the DFT structures of the [Mn^{III}(OO^{t}Bu)(dpaq^{2Me})]$^+$ complex, which also had elongated Mn-N$_{eq}$ and Mn-O bonds relative to **1**.[73] A similar trend was observed in the Mn-O bonds of the [Mn^{III}(OOCm)(^{6Me}dpaq)]$^+$ and [Mn^{III}(OH)(^{6Me}dpaq)]$^+$ complexes (H^{6Me}dpaq = 2-(bis((6-methylpyridin-2-yl)methyl)amino)-N-(quinolin-8-yl)acetamide), where the crystal structures revealed an elongated Mn-O bond in the alkylperoxo species, but with similar Mn-N$_{eq}$ bonds.[70] Additionally, the Mn-O and O-O bond lengths in the DFT structure of **3** fall within the range of those observed in crystal structures of Mn^{III}-alkylperoxo complexes.[71-73] The Mn-O and O-O bond lengths for **3** are both shorter than those of the DFT optimized structure of [Mn^{III}(OOH)(14-TMC)]$^{2+}$, which are 1.93 and 1.52 Å, respectively.[67]

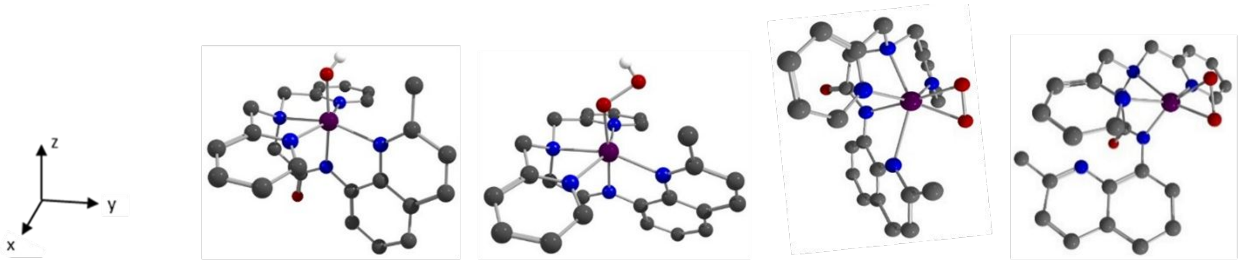

	[Mn^{III}(OH)(dpaq^{2Me})]$^+$ **1**	[Mn^{III}(OOH)(dpaq^{2Me})]$^+$ **3**	[Mn^{III}(O$_2$)(dpaq^{2Me})] **4a** Quinoline Bound	[Mn^{III}(O$_2$)(dpaq^{2Me})] **4b** Quinoline Unbound
Mn-O	1.82	1.86	1.84/1.92	1.84
Mn-N (Qn)	2.19	2.23	2.47	NA
Mn-N (Py)	2.15	2.20	2.28/2.43	2.15
Mn-N (amide)	1.98	1.97	2.09	1.99
O-O	NA	1.47	1.44	1.45

Figure 14. DFT optimized geometries for [Mn^{III}(OOH)(dpaq^{2Me})]$^+$, [Mn^{III}(OH)(dpaq^{2Me})]$^+$, and [Mn^{III}(O$_2$)(dpaq^{2Me})] with the quinoline arm bound **4a** or unbound **4b** along with relevant structural information (bottom). Hydrogen atoms attached to carbons have been removed for clarity.

We performed TD-DFT and CASSCF/NEVPT2 calculations for **1** and **3** to evaluate our assignment of **3** as a Mn^{III}-hydroperoxo species. The TD-DFT calculated spectrum for **1** corresponds well to the experimental spectrum of this complex. Band i of **1**, which arises from a Mn $d_{x^2-y^2} \longrightarrow d_{z^2}$ transition (Figure 15, Table S6) is predicted to be at 778 nm, in excellent agreement with the experimental feature at 780 nm. (The orbital labels use a coordinate system with the z- and x-axes along the Mn-O and Mn-N$_{quinoline}$ bonds, respectively; see Figure 14.) Bands ii and iii in **1** correspond to Mn^{III} $d_{yz} \longrightarrow d_{z^2}$ and $d_{xz} \longrightarrow d_{z^2}$ transitions, respectively (Table S6), and are predicted to occur at 535 and 483 nm. These bands correspond nicely with the broad experimental feature at 515 nm (Figure 15). Electronic transitions calculated by the CASSCF/NEVPT2 method are very similar (Figure S13).

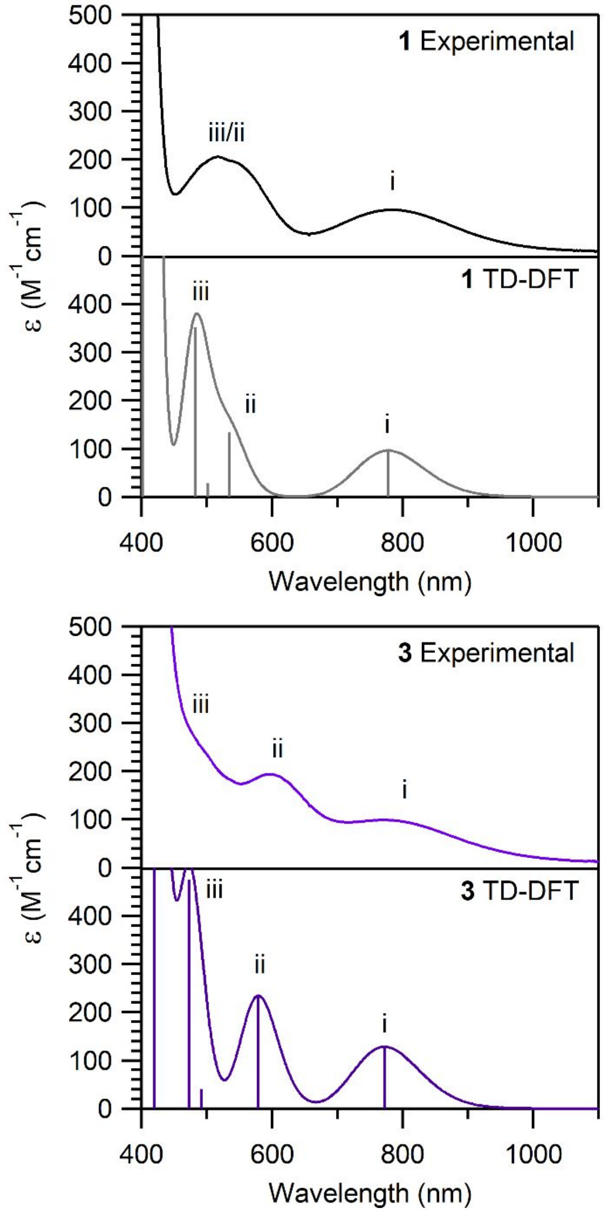

Figure 15. Experimental and TD-DFT electronic absorption spectra for **1** (top) and **3** (bottom).

The TD-DFT and CASSCF/NEVPT2 spectra of **3** are likewise in excellent agreement with experimental data (Figure 15, bottom and Figure S13), predicting absorption features near 770, 580, and 470 nm. In the TD-DFT spectrum for **3**, band i is at slightly higher energy (771 nm) compared to **1** (Figure 15, Table S7). This modest band shift is in excellent agreement with the experimental data, which shows a slight blue shift in the lowest energy band of **3** compared to **1**

(Figure 6). This blue shift in band i, which is due to a $d_{x^2-y^2} \longrightarrow d_{z^2}$ transition, arises from the longer Mn-N_{eq} bond lengths in **3** that stabilize the $d_{x^2-y^2}$ orbital. This orbital stabilization is apparent in the calculated Mn^{III} 3d orbital splitting patterns of **1** and **3** (Figure 16).

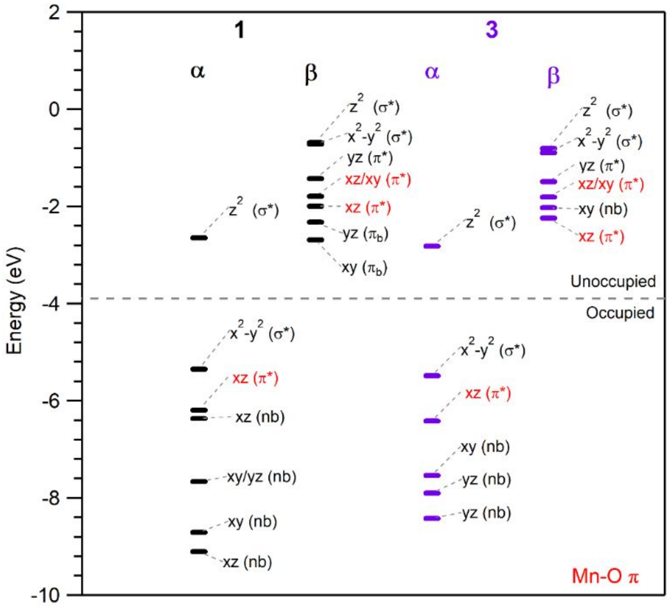

Figure 16. Molecular orbital (MO) energy-level diagrams for **1** (left, black) and **3** (right, purple) complexes from DFT calculations. MOs are labelled based on the most significant contributions.

Bands ii and iii in the TD-DFT absorption spectrum of **3** correspond to Mn $d_{yz} \longrightarrow d_{z^2}$ and Mn $d_{xz} \longrightarrow d_{z^2}$ transitions (Table S7). Both bands are predicted to be lower in energy in **3** relative to **1**, which reproduces the observed shifts in the experimental spectrum (Figures 6 and 15). These shifts are caused by stabilization of the Mn^{III} d_{z^2} orbital due to the elongation of the Mn^{III}-O bond in **3** (Figure 16). The TD-DFT calculations also predict hydroperoxo-to-Mn^{III} charge transfer bands for **3** in the near-UV region (364 nm; see Table S7). The experimental spectra of $[Mn^{III}(OOH)(14\text{-}TMC)]^{2+}$ and $[Mn^{III}(OOH)(13\text{-}TMC)]^{2+}$ have intense UV absorption bands (324 and 384 nm for $[Mn^{III}(OOH)(14\text{-}TMC)]^{2+}$ [67] and 305 and 425 nm for $[Mn^{III}(OOH)(13\text{-}TMC)]^{2+}$).[66] On the basis of our TD-DFT computations for **3**, these bands could arise form hydroperoxo-to-Mn^{III} charge transfer transitions.

Because the TD-DFT computations nicely reproduce the experimental electronic absorption spectrum of **3**, we used this method to examine the frontier MOs of the Mn^{III}-hydroperoxo unit and compare them with the Mn^{III}-hydroxo analogue **1**. In each complex, the Mn^{III} d_{xz} MO is involved in π-interactions with the axial ligand (hydroxo for **1** and hydroperoxo for **3**). The Mn^{III} d_{xz} MO for **3** has a significant contribution (41.2%) from the O-O π* MO of the hydroperoxo moiety, indicating strong Mn-OOH π-interactions, and a small admixture (1.9%) of N$_{amide}$ character from the N $2p_z$ orbital (Figure 17, bottom-right, and Tables S4 and S5). The Mn^{III} d_{xz} MO of **1** reveals strong π-mixing with the hydroxo ligand, with 28% O character from a 2p orbital of the O atom. This MO contains a small amount (1.7%) of N$_{amide}$ character from the N p_x orbital (see Figure 17, top-right and Tables S2 and S3). Overall, the computations indicate greater π-covalency in the Mn^{III}-hydroperoxo complex. An examination of the Mn^{III} d_z^2 MOs of **1** and **3** allow us to examine σ-interactions with the hydroxo and hydroperoxo ligands. In **1**, there is a modest contribution (8.7%) from a 2p orbital of the hydroxo oxygen (Table S2). In **3**, the d_z^2 orbital shows a larger σ-interaction, with a 14.1% contribution from the in-plane O-O π* orbital of the hydroperoxo group (Table S4). The d_z^2 MOs of both **1** and **3** contain similar contributions from the N$_{amide}$ function (5.7% and 5.8% respectively, Tables S2 and S4). Taken together, the DFT computations predict the Mn^{III}-hydroperoxo bonding to be more covalent than the Mn^{III}-hydroxo bonding.

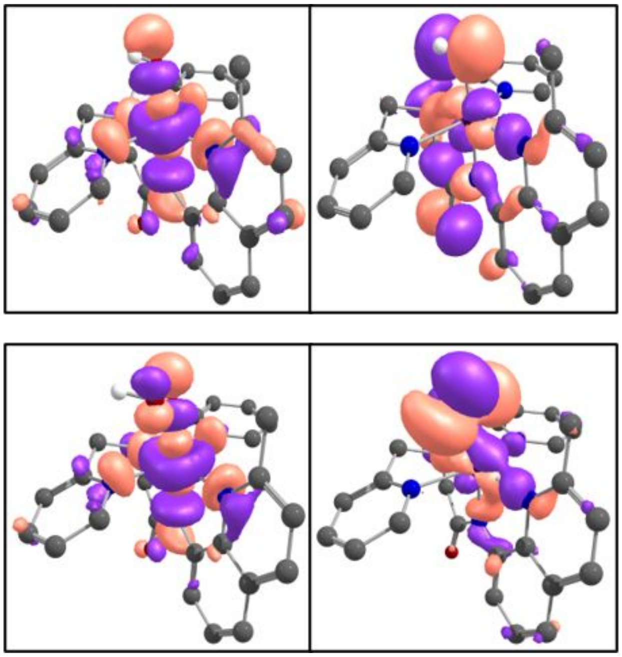

Figure 17. Surface contour plots of the spin up d_{z^2} (left) and d_{xz} (right) MOs of **1** (top) and **3** (bottom).

B) DFT Calculations for 4. DFT studies were performed on two potential structures of **4** to determine which is more consistent with experimental data. We considered a seven-coordinate structure with a side-on peroxo ligand and pentadentate dpaq^{2Me} (**4a**) and a six-coordinate structure with a side-on peroxo unit and a tetradentate dpaq^{2Me} ligand (**4b**). The tetradentate structure was achieved by rotating the quinoline moiety so that it was unable to coordinate the Mn center. The optimized geometries and key structural parameters of both structures are in Figure 14. In the seven-coordinate model **4a**, the Mn^{III}-peroxo and Mn^{III}-pyridine bonds are asymmetric (Mn-O of 1.84 and 1.92 Å and Mn-N of 2.28 and 2.43 Å). The N$_{pyridine}$-Mn^{III}-N$_{pyridine}$ bond angle of **4a** of 146.3° is slightly smaller than that in **1** (155.2°). Additionally, the Mn-quinoline bond distance is quite long (2.47 Å), with the quinoline tilted toward one pyridine group (Figure 14). This tilt is manifested by an asymmetry in the N$_{quinoline}$-Mn-N$_{pyridine}$ bond angles (116.4° and 88.1°). For comparison, these angles are quite similar (106.0° and 98.1°) in **1**. The asymmetry in **4a** could appear at odds with the ^{1}H NMR data for **4**, as inequivalent pyridines would give rise to a greater number of proton resonances. However, many of the peaks tentatively assigned as pyridine protons are broadened considerably compared to that of **1** (Figure 13), which could be explained by averaging of slightly dissimilar pyridine moieties.[101]

In the six-coordinate structure **4b**, a rotation of the quinoline arm prevents any association between the quinoline nitrogen and the manganese. This structure is quite similar to other DFT and crystallographic structures of 6-coordinate Mn^{III}-peroxo species, with the Mn-N bonds all bent considerably to accommodate the side-on peroxo unit.[54-55, 57-58, 62, 64, 106] In this case, the Mn^{III}-peroxo and Mn^{III}-$N_{pyridine}$ bond lengths are symmetric at 1.84 and 2.15 Å, respectively (Figure 14).

To distinguish between these potential structures, we calculated total energies and spectroscopic properties using both DFT and CASSCF/NEVPT2 methods. Both the DFT and CASSCF/NEVPT2 computations predict **4a** to be lower in energy (by 3 and 10 kcal mol^{-1}). The calculated spectroscopic properties for **4a** and **4b** are very similar and both are in reasonable agreement with experiment (Figures S14 and S15). Thus, while the predicted spectroscopic data for either structure are compatible with experiment, the lower energy for **4a** leads us to favor this structure. The significant distortion of the ligand in the structure of **4a** could explain the inability of this complex to react with acid to form **3**.

Reactivity of 3 and 4. Having assessed the formulations of **3** and **4** using a combination of spectroscopic and computational methods, we next analyzed the chemical reactivity of these complexes. We focused on substrates known to react with previously reported Mn^{III}-hydroperoxo and Mn^{III}-peroxo complexes.[57, 60, 62, 65-67, 106-107]

A) Reactivity of 3 with Thioanisole. The two previously reported Mn^{III}-hydroperoxo species, $[Mn^{III}(OOH)(14\text{-}TMC)]^{2+}$ [67] and $[Mn^{III}(OOH)(13\text{-}TMC)]^{2+}$,[66] reacted rapidly with thioanisole to give sulfoxidation products. Only $[Mn^{III}(OOH)(13\text{-}TMC)]^{2+}$ showed reactivity towards hydrocarbons (C-H bond activation).[66] Such limited reactivity has also been observed for Fe^{III}-hydroperoxo species, which show reactivity towards thioanisole,[108-109] while reactions with hydrocarbons[108] or other substrates[110] are rarer. The addition of thioanisole to **3** resulted in unexpected behavior. When 10 equiv. thioanisole were added to a 1.25 mM solution of **3**, the absorption bands did not decay, suggesting the lack of a direct reaction. Instead, the presence of thioanisole in the solution prolonged the slow decay phase of **3** from 1200 to 2000 seconds (Figure 19, top). After 2000 seconds, the absorption band at 610 nm rapidly lost intensity and began to increase in intensity again after an additional 360 seconds (Figure 18, top). This extended decay was also observed after the addition of 5 equiv. 4-methoxythioanisole (Figure 18, bottom). In the presence of 4-methoxythioanisole, the slow decay phase of the feature at 610 nm is prolonged to 2500 seconds. After 2500 seconds, this feature decays rapidly and begins increasing in intensity after approximately 500 seconds (Figure 18, bottom).

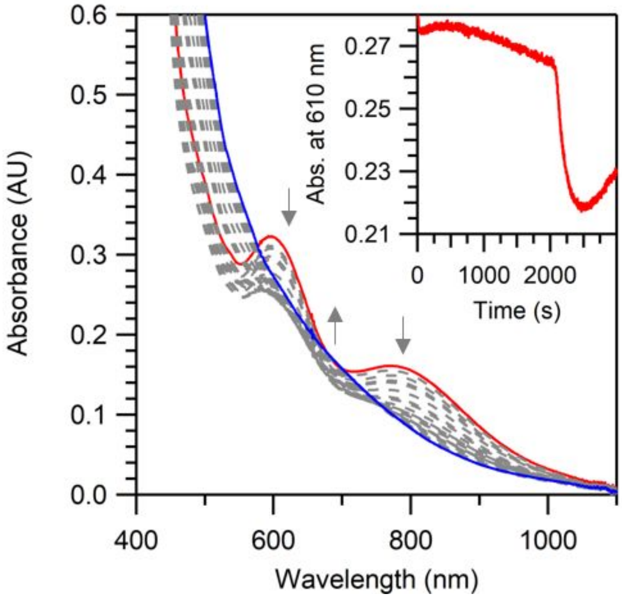

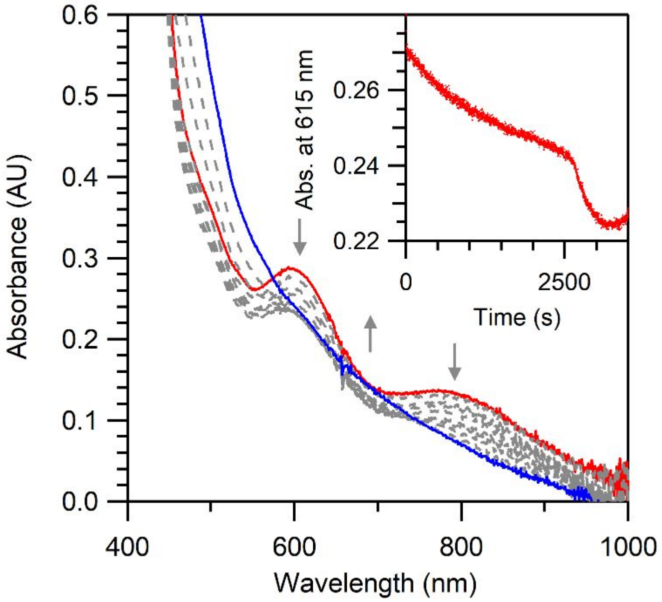

Figure 18. Top: Electronic absorption spectra of a 1.25 mM solution of **3** (red trace) after the addition of 10 equiv. thioanisole (blue trace) in MeCN at -40°C. Significant decay of **3** was not observed until after approximately 2000 seconds (inset). Bottom: Electronic absorption spectra of a 1.25 mM solution of **3** (red trace) after the addition of 5 equiv. 4-methoxythioanisole (blue trace) in MeCN at -40°C. Significant decay of **3** was not observed until after approximately 2500 seconds (inset).

^{1}H NMR experiments following these reactions reveal 1-methoxy-4-(methylsulfinyl)benzene and unoxidized 4-methoxythioaniole in a 0.25:0.75 ratio (Figure S16). The presence of oxidized products in conjunction with the altered decay profile indicates that **3** is not the active oxidant. The extended lifetime of **3** in the presence of 4-methoxythioanisole could suggest that the active oxidant is an unobserved intermediate that forms during the self-decay of **3**. This intermediate reacts with 4-methoxythioanisole, delaying the accumulation necessary to initiate the rapid decay of **3**. Alternatively, 4-methoxythioanisole could intercept excess H_2O_2 in solution, and this reaction could also slow the decay of **3**. Control experiments lacking **3** reveal that excess hydrogen peroxide is capable of oxidizing 4-methoxythioanisole to 1-methoxy-4-(methylsulfinyl)benzene in a similar yield (Figure S16).

The lack of a direct reaction between **3** and substrates contrasts with the previous reports of Mn^{III}-hydroperoxo species with nonporphyrin ligands. Those complexes reacted directly with thioanisole and, in one case, hydrocarbons.[66-67] However, there is precedent for Fe^{III}-hydroperoxo species serving as precursors to active oxidants rather than acting as the oxidant themselves. While there are some examples of direct substrate oxidation by Fe^{III}-hydroperoxo complexes,[109, 111-112] these reactions are quite slow compared to those of their Fe-oxo counterparts.[99, 110, 113-114]

B) Reactivity of 4 with cyclohexanecarboxaldehyde. The reactivity of **4** towards substrates was also explored. For these studies, **4** was treated with 100 equiv. substrate and any reaction was monitored by electronic absorption spectroscopy. This complex was not reactive towards substrates with weak C-H or O-H bonds (9,10-dihydroanthracene, 1,4-cyclohexadiene, 2,4,6-tri-*tert*-butylphenol, and TEMPOH) (Figure S17), but **4** did show reactivity towards cyclohexanecarboxaldehyde (CCA; see Figure 19), a common substrate for Mn^{III}-peroxo complexes.[60, 65, 106, 115] For the reaction with CCA, the decay could be fit to a pseudo-first order model. Data collected at several concentrations of CCA allowed us to determine a second order rate constant of 0.07 $M^{-1}s^{-1}$ at -40 ℃ (Figure 19). This rate constant is similar to those reported for the reaction of CCA with [Mn^{III}(O$_2$)(13-TMC)]$^+$ and [Mn^{III}(O$_2$)(14-TMC)]$^+$ (0.2 and 0.4 $M^{-1}s^{-1}$) at 10 ℃,[52, 60] but slower than that observed for other Mn^{III}-peroxo complexes supported by aminopyridyl ligands (0.19 to 3.1 $M^{-1}s^{-1}$ at -40 ℃).[53] The lack of reactivity of **4** towards substrates with weak C-H or O-H bonds is also consistent with reports for other Mn^{III}-peroxo species.[57, 59, 61-62, 65, 107] Collectively, **4** shows reactivity in keeping with its assignment as a Mn^{III}-peroxo complex.

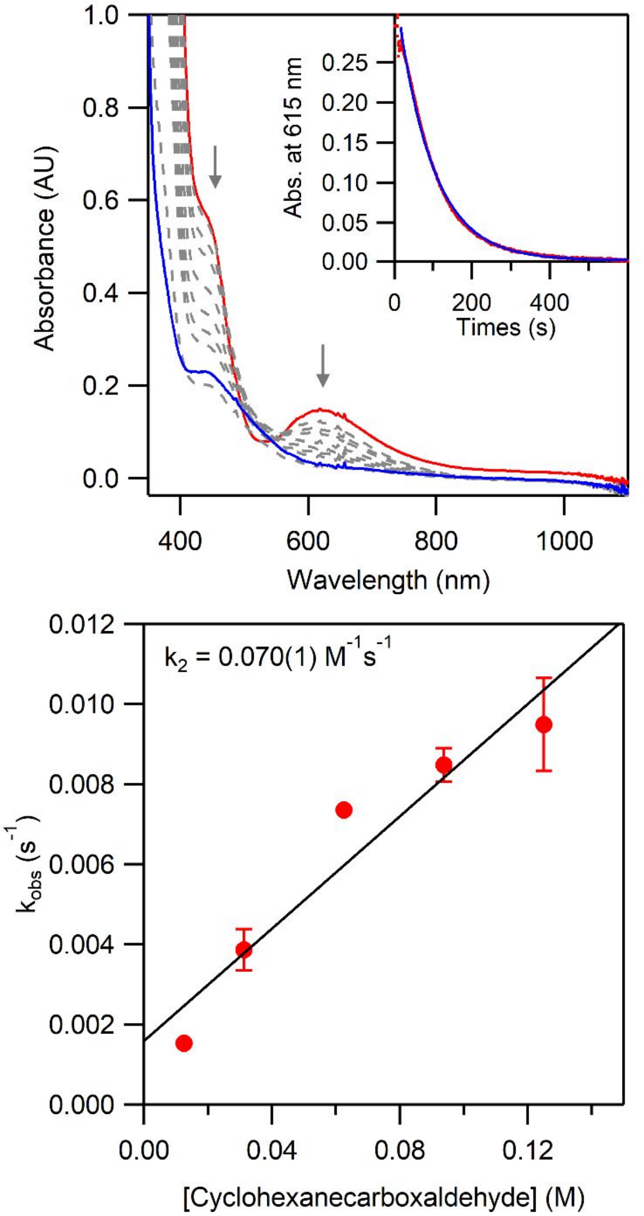

Figure 19. Top: Electronic absorption spectra for a solution of **4** (red trace) after addition of 100 equivalents of CCA at -40°C. The feature at 615 nm decays completely to the blue trace. Inset: Decay trace of the feature at 615 nm over time. Bottom: Plot of k_{obs} vs. substrate concentration for the reaction of **4** with cyclohexane carboxaldehyde.

Summary and Conclusions

Manganese catalysts in both biological and synthetic systems facilitate oxidation-reduction reactions through the formation and decay of peroxo intermediates. While there are now numerous examples of side-on Mn^{III}-peroxo complexes, end-on Mn^{III}-hydroperoxo species remain relatively scarce. Such complexes are critical intermediates in H_2O_2-activating Mn catalysts that effect an array of impressive substrate oxidation reactions. Consequently, our present understanding of the mechanisms of a broad class of synthetic Mn catalysts is stymied by the paucity of Mn^{III}-hydroperoxo complexes.

In this present work, we have accessed several different intermediates from the reaction of the Mn^{III}-hydroxo complex **1** with H_2O_2, controlling the particular intermediate formed by introducing acid or base to the reaction mixture. These new species, which we assign as $[Mn^{III}Mn^{IV}(\mu\text{-}O)_2(dpaq^{2Me})_2]^+$ (**2**), $[Mn^{III}(OOH)(dpaq^{2Me})]^+$ (**3**), and $[Mn^{III}(O_2)(dpaq^{2Me})]$ (**4**), can also interconvert by thermal decay and/ or acid-base reactions (Scheme 5). In the absence of acid or base, the reaction of **1** with H_2O_2 yields a fleeting Mn^{III}-hydroperoxo intermediate **3** that is observed before the formation of the bis(μ-oxo)dimanganese(III,IV) complex **2** (Figure 1). This dinuclear complex decays to quantitatively regenerate **1**. While the reductant for this latter process is unclear, the reaction solution contains an excess of H_2O_2 (10 equiv. relative to the initial concentration of **1**), which could aid in the conversion of **2** to **1**.

Scheme 5. Summary of the reactions of a Mn^{III}-hydroxo complex with H_2O_2 under various conditions. The reactions are not balanced but indicate the Mn complexes detected by spectroscopic methods.

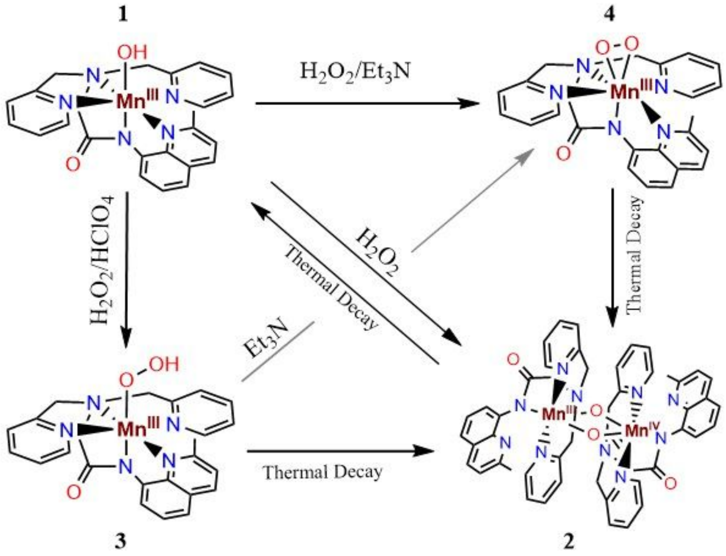

The fleeting Mn^{III}-hydroperoxo complex **3** can be stabilized in the presence of acid, permitting its characterization. ^{1}H NMR, XAS, and ESI-MS data for **3** are consistent with its assignment as a mononuclear Mn^{III}-hydroperoxo species with a geometry very similar to that of **1**. DFT and CASSCF/NEVPT2 computations for [Mn^{III}(OOH)(dpaq^{2Me})]$^+$ nicely reproduce the UV-vis spectrum for **3**, and **3** reacts with base to give the Mn^{III}-peroxo complex **4**. While vibrational data would bolster the assignments of both **3** and **4**, the weak electronic absorption bands of these compounds are poorly suited for resonance Raman experiments. IR experiments have been unsuccessful, likely due to the low thermal stability of these species. Nonetheless, spectroscopic and reactivity profiles corroborate the assignment of **3** as a Mn^{III}-hydroperoxo complex.

While the deprotonation of the Mn^{III}-hydroperoxo species **3** to give its side-on Mn^{III}-peroxo counterpart **4** by the addition of base follows reactivity reported for Mn^{III}-hydroperoxo species,[66-67] its conversion of to the bis(μ-oxo)dimanganese(III,IV) complex **2** via thermal decay is, to the best of our knowledge, unprecedented. Nonetheless, the thermal decay of **3** to **2** mimics a step in the proposed mechanism for manganese ribonucleotide reductase, where an Mn^{II}Mn^{III}-OOH intermediate decays to give a bis(μ-oxo)dimanganese(III,IV) center.[3] A previous study of the related complex [Mn^{III}(OH)(dpaq)]$^+$ with H_2O_2 revealed the formation of a bis(μ-oxo)dimanganese(III,IV) similar to **2**.[77] However, in that case no intermediates were observed en route to **3**, and no mononuclear Mn^{III}-peroxo or Mn^{III}-hydroperoxo complexes were reported. The sole difference between the dpaq ligand used in that study and the dpaq^{2Me} ligand employed here is the presence of the 2-methyl-quinolinyl group that places steric bulk near the coordinate site that accommodates peroxo, hydroperoxo, or oxo ligands. We propose that the introduction of this steric bulk tends to disfavor, but not completely suppress, the formation of dinuclear complexes, allowing us to trap unstable, mononuclear intermediates. In support, previous studies from our lab revealed differences in the dioxygen activation mechanisms of $[Mn^{II}(NCMe)(dpaq)]^+$ and $[Mn^{II}(NCMe)(dpaq^{2Me})]^+$.[116] The O_2 activation mechanism of the former complex, with the less bulky dpaq ligand, involves dinuclear intermediates, while the mechanism of the latter complex, with the bulky $dpaq^{2Me}$ ligand, involved only mononuclear species. This present work is thus a further example of how relatively modest steric effects can be leveraged to permit the observation of new intermediates.

To the best of our knowledge, the reaction of **1** with H_2O_2 to give **3** is the first report of the generation of a Mn^{III}-OOH species via the direct reaction of a manganese(III) center with H_2O_2. The isosbestic points observed when this reaction is monitored by UV-vis spectroscopy (Figure 6, top) suggest a simple ligand substitution reaction, aided by acid. This reaction mimics a key step proposed for H_2O_2-activating Mn catalysts, where a Mn^{III}-OOH intermediate forms via the binding of H_2O_2 to a Mn^{III}-OH center.[24, 28, 43-45] In the catalytic systems, the next step in the mechanism is heterolytic cleavage of the O-O bond, which is promoted by a carboxylic acid coordinated to the Mn^{III} center in an orientation *cis* to the hydroperoxo ligand.[24, 28] As **3** features a Mn^{III}-OOH unit supported by a pentadentate ligand, there is no binding site for a carboxylic acid. Moreover, the decay process of **3** to give the bis(μ-oxo)dimanganese(III,IV) species **2** is complex, consisting of several phases (Figure 6, bottom). The observation that certain substrates slow the decay of **3** points to the formation of some reactive, yet unidentified, intermediate. Future studies will aim to better understand this decay process and uncover the roles of the ligand environment and reaction conditions in modulating this process.

Supplementary Information Available: Electronic absorption spectra, EPR spectra, ^1H NMR spectra, description of CASSCF results, DFT orbital compositions and electron density difference maps, and Cartesian coordinates for optimized structures.

Conflicts of interest: There are no conflicts to declare.

Acknowledgements. This work was supported by funding provided by the U.S. NSF CHE-2154955 to T. A. J. The U.S. NSF is also acknowledged for funds used to support the purchase of EPR instrumentation (CHE-0946883). Some of the calculations were performed at the University of Kansas Center for Research Computing (CRC), including the BigJay Cluster resource funded through U.S. NSF grant MRI-2117449. The NIH is acknowledged for funds used to support NMR instrumentation (Shared Instrumentation Grant # S10OD016360). Use of the Stanford Synchrotron Radiation Lightsource, SLAC National Accelerator Laboratory, is supported by the U.S. Department of Energy, Office of Science, Office of Basic Energy Sciences under Contract No. DE-AC02-76SF00515. The SSRL Structural Molecular Biology Program is supported by the DOE Office of Biological and Environmental Research, and by the National Institutes of Health, National Institute of General Medical Sciences (including P41GM103393). The contents of this publication are solely the responsibility of the authors and do not necessarily represent the official views of NIGMS or NIH. Computational aspects of this work were supported by the high-performance computing (HPC) facilities operated by the Center for Research Computing at the University of Kansas.

References

1. Leto, D. F.; Jackson, T. A., Peroxomanganese complexes as an aid to understanding redox-active manganese enzymes. *J. Biol. Inorg. Chem.* **2014,** *19*, 1-15.
2. Fiedler, A. T.; Fischer, A. A., Oxygen activation by mononuclear Mn, Co, and Ni centers in biology and synthetic complexes. *J. Biol. Inorg. Chem.* **2017,** *22* (2), 407-424.
3. Cotruvo, J. A.; Stich, T. A.; Britt, R. D.; Stubbe, J., Mechanism of Assembly of the Dimanganese-Tyrosyl Radical Cofactor of Class Ib Ribonucleotide Reductase: Enzymatic Generation of Superoxide Is Required for Tyrosine Oxidation via a Mn(III)Mn(IV) Intermediate. *J. Am. Chem. Soc.* **2013,** *135* (4027-4039).

4. Boal, A. K.; Cotruvo, J. A.; Stubbe, J.; Rosenzweig, A. C., Structural Basis for Activation of Class Ib Ribonucleotide Reductase. *Science* **2010,** *329* (5998), 1526-1530.
5. Cotruvo, J. A., Jr.; Stubbe, J., NrdI, a flavodoxin involved in maintenance of the diferric-tyrosyl radical cofactor in Escherichia coli class Ib ribonucleotide reductase. *Proc. Natl. Acad. Sci. U.S.A.* **2008,** *105* (38), 14383-8.
6. Cotruvo, J. A.; Stubbe, J., Escherichia coli Class Ib Ribonucleotide Reductase Contains a Dimanganese(III)-Tyrosyl Radical Cofactor in Vivo. *Biochemistry* **2011,** *50* (10), 1672-1681.
7. Gunderson, W. A.; Zatsman, A. I.; Emerson, J. P.; Farquhar, E. R.; Que, L.; Lipscomb, J. D.; Hendrich, M. P., Electron Paramagnetic Resonance Detection of Intermediates in the Enzymatic Cycle of an Extradiol Dioxygenase. *J. Am. Chem. Soc.* **2008,** *130* (44), 14465-14467.
8. Glickman, M. H.; Klinman, J. P., Nature of Rate-Limiting Steps in the Soybean Lipoxygenase-1 Reaction. *Biochemistry* **1995,** *34* (43), 14077-14092.
9. Su, C.; Sahlin, M.; Oliw, E. H., Kinetics of Manganese Lipoxygenase with a Catalytic Mononuclear Redox Center. *J. Biol. Inorg. Chem.* **2000,** *275* (25), 18830-18835.
10. Wennman, A.; Karkehabadi, S.; Oliw, E. H., Kinetic investigation of the rate-limiting step of manganese- and iron-lipoxygenases. *Arch. Biochem. Biphys.* **2014,** *555–556*, 9-15.
11. Wennman, A.; Oliw, E. H.; Karkehabadi, S.; Chen, Y., Crystal Structure of Manganese Lipoxygenase of the Rice Blast Fungus Magnaporthe oryzae. *J. Biol. Chem.* **2016**.
12. Sheng, Y.; Butler Gralla, E.; Schumacher, M.; Cascio, D.; Cabelli, D. E.; Selverstone Valentine, J., Six-coordinate manganese(3+) in catalysis by yeast manganese superoxide dismutase. *Proc. Natl. Acad. Sci. U.S.A.* **2012,** *109* (36), 14314-14319.
13. Bull, C.; Niederhoffer, E. C.; Yoshida, T.; Fee, J. A., Kinetic-Studies of Superoxide Dismutases - Properties of the Manganese-Containing Protein from Thermus-Thermophilus. *J. Am. Chem. Soc.* **1991,** *113* (11), 4069-4076.
14. Hearn, A. S.; Tu, C. K.; Nick, H. S.; Silverman, D. N., Characterization of the Product Inhibited Complex in Catalysis by Human Manganese Superoxide Dismutase. *J. Biol. Chem.* **1999,** *274* (35), 24457-24460.
15. Jackson, T. A.; Karapetian, A.; Miller, A.-F.; Brunold, T. C., Probing the Geometric and Electronic Structures of the Low-Temperature Azide Adduct and the Product-Inhibited Form of Oxidized Manganese Superoxide Dismutase. *Biochemistry* **2005,** *44* (5), 1504-1520.
16. Abreu, I. A.; Rodriguez, J. A.; Cabelli, D. E., Theoretical Studies of Manganese and Iron Superoxide Dismutases: Superoxide Binding and Superoxide Oxidation. *J. Phys. Chem. B* **2005,** *109* (51), 24502-24509.
17. Carrasco, R.; Morgenstern-Badarau, I.; Cano, J., Two proton-one electron coupled transfer in iron and manganese superoxide dismutases: A density functional study. *Inorg. Chim. Acta* **2007,** *360* (1), 91-101.
18. McEvoy, J. P.; Brudvig, G. W., Water-Splitting Chemistry of Photosystem II. *Chem. Rev.* **2006,** *106* (11), 4455-4483.
19. Cox, N.; Pantazis, D. A.; Neese, F.; Lubitz, W., Biological Water Oxidation. *Acc. Chem. Res.* **2013,** *46* (7), 1588-1596.
20. Wang, J.; Askerka, M.; Brudvig, G. W.; Batista, V. S., Crystallographic Data Support the Carousel Mechanism of Water Supply to the Oxygen-Evolving Complex of Photosystem II. *ACS Energy Lett.* **2017,** *2* (10), 2299-2306.

21. Siegbahn, P. E. M., O-O Bond Formation in the S4 State of the Oxygen-Evolving Complex in Photosystem II. *Chem. Eur. J.l* **2006,** *12* (36), 9217-9227.
22. Suga, M.; Akita, F.; Sugahara, M.; Kubo, M.; Nakajima, Y.; Nakane, T.; Yamashita, K.; Umena, Y.; Nakabayashi, M.; Yamane, T.; Nakano, T.; Suzuki, M.; Masuda, T.; Inoue, S.; Kimura, T.; Nomura, T.; Yonekura, S.; Yu, L.-J.; Sakamoto, T.; Motomura, T.; Chen, J.-H.; Kato, Y.; Noguchi, T.; Tono, K.; Joti, Y.; Kameshima, T.; Hatsui, T.; Nango, E.; Tanaka, R.; Naitow, H.; Matsuura, Y.; Yamashita, A.; Yamamoto, M.; Nureki, O.; Yabashi, M.; Ishikawa, T.; Iwata, S.; Shen, J.-R., Light-induced structural changes and the site of O=O bond formation in PSII caught by XFEL. *Nature* **2017,** *543*, 131.
23. Schuth, N.; Zaharieva, I.; Chernev, P.; Berggren, G.; Anderlund, M.; Styring, S.; Dau, H.; Haumann, M., Kα X-ray Emission Spectroscopy on the Photosynthetic Oxygen-Evolving Complex Supports Manganese Oxidation and Water Binding in the S3 State. *Inorg. Chem.* **2018,** *57* (16), 10424-10430.
24. Bryliakov, K. P.; Talsi, E. P., Active sites and mechanisms of bioinspired oxidation with H2O2, catalyzed by non-heme Fe and related Mn complexes. *Coord. Chem. Rev.s* **2014,** *276*, 73-96.
25. Baglia, R. A.; Zaragoza, J. P. T.; Goldberg, D. P., Biomimetic Reactivity of Oxygen-Derived Manganese and Iron Porphyrinoid Complexes. *Chem. Rev.* **2017,** *117* (21), 13320-13352.
26. Qiu, B.; Xu, D.; Sun, Q.; Miao, C.; Lee, Y.-M.; Li, X.-X.; Nam, W.; Sun, W., Highly Enantioselective Oxidation of Spirocyclic Hydrocarbons by Bioinspired Manganese Catalysts and Hydrogen Peroxide. *ACS Catal.* **2018,** *8* (3), 2479-2487.
27. Huang, Z.; Guan, R.; Shanmugam, M.; Bennett, E. L.; Robertson, C. M.; Brookfield, A.; McInnes, E. J. L.; Xiao, J., Oxidative Cleavage of Alkenes by O2 with a Non-Heme Manganese Catalyst. *J. Am. Chem. Soc.* **2021,** *143* (26), 10005-10013.
28. Vicens, L.; Olivo, G.; Costas, M., Rational Design of Bioinspired Catalysts for Selective Oxidations. *ACS Catal.* **2020,** *10* (15), 8611-8631.
29. Yang, J.; Wang, L.; Lv, Y.; Li, N.; An, Y.; Gao, S., Oxidative kinetic resolution of heterocyclic sulfoxides with a porphyrin-inspired manganese complex by hydrogen peroxide. *Tet. Lett.* **2018,** *59* (2), 156-159.
30. Chen, J.; Jiang, Z.; Fukuzumi, S.; Nam, W.; Wang, B., Artificial nonheme iron and manganese oxygenases for enantioselective olefin epoxidation and alkane hydroxylation reactions. *Coord. Chem. Rev.* **2020,** *421*.
31. Milan, M.; Bietti, M.; Costas, M., Enantioselective aliphatic C-H bond oxidation catalyzed by bioinspired complexes. *Chem. Commun.* **2018,** *54* (69), 9559-9570.
32. Masferrer-Rius, E.; Borrell, M.; Lutz, M.; Costas, M.; Klein Gebbink, R. J. M., Aromatic C−H Hydroxylation Reactions with Hydrogen Peroxide Catalyzed by Bulky Manganese Complexes. *Adv. Synth. Catal.* **2021,** *363* (15), 3783-3795.
33. Dantignana, V.; Milan, M.; Cusso, O.; Company, A.; Bietti, M.; Costas, M., Chemoselective Aliphatic C-H Bond Oxidation Enabled by Polarity Reversal. *ACS Cent. Sci.* **2017,** *3* (12), 1350-1358.
34. Ottenbacher, R. V.; Talsi, E. P.; Bryliakov, K. P., Mechanism of Selective C–H Hydroxylation Mediated by Manganese Aminopyridine Enzyme Models. *ACS Catal.***2014,** *5* (1), 39-44.
35. Battioni, P.; Renaud, J. P.; Bartoli, J. F.; Reina-Artiles, M.; Fort, M.; Mansuy, D., Monooxygenase-like oxidation of hydrocarbons by hydrogen peroxide catalyzed by

manganese porphyrins and imidazole: selection of the best catalytic system and nature of the active oxygen species. *J. Am. Chem. Soc.* **2002,** *110* (25), 8462-8470.

36. Ottenbacher, R. V.; Samsonenko, D. G.; Talsi, E. P.; Bryliakov, K. P., Highly Enantioselective Bioinspired Epoxidation of Electron-Deficient Olefins with H2O2 on Aminopyridine Mn Catalysts. *ACS Catal.* **2014,** *4* (5), 1599-1606.
37. Lyakin, O. Y.; Ottenbacher, R. V.; Bryliakov, K. P.; Talsi, E. P., Asymmetric Epoxidations with H2O2 on Fe and Mn Aminopyridine Catalysts: Probing the Nature of Active Species by Combined Electron Paramagnetic Resonance and Enantioselectivity Study. *ACS Catal.* **2012,** *2* (6), 1196-1202.
38. Xu, D.; Sun, Q.; Lin, J.; Sun, W., Ligand regulation for manganese-catalyzed enantioselective epoxidation of olefins without acid. *Chem. Commun.* **2020,** *56* (86), 13101-13104.
39. Miao, C.; Yan, X.; Xu, D.; Xia, C.; Sun, W., Bioinspired Manganese Complexes and Graphene Oxide Synergistically Catalyzed Asymmetric Epoxidation of Olefins with Aqueous Hydrogen Peroxide. *Adv. Synth. Catal.* **2017,** *359* (3), 476-484.
40. Chen, X.; Gao, B.; Su, Y.; Huang, H., Enantioselective Epoxidation of Electron-Deficient Alkenes Catalyzed by Manganese Complexes with Chiral N4 Ligands Derived from Rigid Chiral Diamines. *Adv. Synth. Catal.* **2017,** *359* (15), 2535-2541.
41. Robinson-Miller, A. P.; Wyatt, M. F.; Tétard, D., Epoxidation of strained alkenes catalysed by (1,2-dimethyl-4(1H)pyridinone-3-olate)2MnIIICl. *J. Mol. Cat. A: Chemical* **2015,** *398*, 376-390.
42. Xing, Q.; Hao, Z.; Hou, J.; Li, G.; Gao, Z.; Gou, J.; Li, C.; Yu, B., Manganese-Catalyzed Achmatowicz Rearrangement Using Green Oxidant H2O2. *J. Org. Chem.* **2021,** *86* (14), 9563-9586.
43. Dai, W.; Shang, S.; Chen, B.; Li, G.; Wang, L.; Ren, L.; Gao, S., Asymmetric epoxidation of olefins with hydrogen peroxide by an in situ-formed manganese complex. *J. Org. Chem.* **2014,** *79* (14), 6688-94.
44. Dai, W.; Li, G.; Wang, L.; Chen, B.; Shang, S.; Lv, Y.; Gao, S., Enantioselective oxidation of sulfides with H2O2 catalyzed by a pre-formed manganese complex. *RSC Adv.* **2014,** *4* (87), 46545-46554.
45. Du, J.; Miao, C.; Xia, C.; Lee, Y.-M.; Nam, W.; Sun, W., Mechanistic Insights into the Enantioselective Epoxidation of Olefins by Bioinspired Manganese Complexes: Role of Carboxylic Acid and Nature of Active Oxidant. *ACS Catal.* **2018,** *8* (5), 4528-4538.
46. Miao, C.; Wang, B.; Wang, Y.; Xia, C.; Lee, Y. M.; Nam, W.; Sun, W., Proton-Promoted and Anion-Enhanced Epoxidation of Olefins by Hydrogen Peroxide in the Presence of Nonheme Manganese Catalysts. *J. Am. Chem. Soc.* **2016,** *138* (3), 936-43.
47. Lin, J.; Miao, C.; Wang, F.; Yang, P.; Sun, Q.; Sun, W., Effect of Ligand Topology on the Reactivity of Chiral Tetradentate Aminopyridine Manganese Complexes. *ACS Cat.s* **2020,** *10* (20), 11857-11863.
48. Ottenbacher, R. V.; Samsonenko, D. G.; Talsi, E. P.; Bryliakov, K. P., Enantioselective Epoxidations of Olefins with Various Oxidants on Bioinspired Mn Complexes: Evidence for Different Mechanisms and Chiral Additive Amplification. *ACS Catal.* **2016,** *6* (2), 979-988.
49. Mohammed, T. P.; Sankaralingam, M., Reactivities of high valent manganese-oxo porphyrins in aqueous medium. *Tetrahedron* **2021**.

50. Shook, R. L.; Peterson, S. M.; Greaves, J.; Moore, C.; Rheingold, A. L.; Borovik, A. S., Catalytic Reduction of Dioxygen to Water with a Monomeric Manganese Complex at Room Temperature. *J. Am. Chem. Soc.* **2011,** *133* (15), 5810-5817.
51. Kitajima, N.; Komatsuzaki, H.; Hikichi, S.; Osawa, M.; Moro-oka, Y., A Monomeric Side-On Peroxo Manganese(III) Complex: Mn(O_2)(3,5-iPr$_2$pzH)(HB(3,5-iPr$_2$pz)$_3$). *J. Am. Chem. Soc.* **1994,** *116*, 11596-11597.
52. Annaraj, J.; Cho, J.; Lee, Y.-M.; Kim, S. Y.; Latifi, R.; de Visser, S. P.; Nam, W., Structural Characterization and Remarkable Axial Ligand Effect on the Nucleophilic Reactivity of a Nonheme Manganese(III)-Peroxo Complex. *Angew. Chem. Int. Ed.* **2009,** *48* (23), 4150-4153.
53. Geiger, R. A.; Chattopadhyay, S.; Day, V. W.; Jackson, T. A., A Series of Peroxomanganese(III) Complexes Supported by Tetradentate Aminopyridyl Ligands: Detailed Spectroscopic and Computational Studies. *J. Am. Chem. Soc.* **2010,** *132* (8), 2821-2831.
54. Geiger, R. A.; Leto, D. F.; Chattopadhyay, S.; Dorlet, P.; Anxolabéhère-Mallart, E.; Jackson, T. A., Geometric and Electronic Structures of Peroxomanganese(III) Complexes Supported by Pentadentate Amino-Pyridine and -Imidazole Ligands. *Inorg. Chem.* **2011,** *50* (20), 10190-10203.
55. Colmer, H. E.; Geiger, R. A.; Leto, D. F.; Wijeratne, G. B.; Day, V. W.; Jackson, T. A., Geometric and electronic structure of a peroxomanganese(iii) complex supported by a scorpionate ligand. *Dalton Trans.* **2014,** *43* (48), 17949-17963.
56. Geiger, R. A.; Wijeratne, G.; Day, V. W.; Jackson, T. A., Steric and Electronic Influences on the Structures of Peroxomanganese(III) Complexes Supported by Tetradentate Ligands. *Eur. J. Inorg. Chem.* **2012**, 1598-1608.
57. Du, J.; Xu, D.; Zhang, C.; Xia, C.; Wang, Y.; Sun, W., Synthesis, characterization, and reactivity of a side-on manganese(iii)–peroxo complex bearing a pentadentate aminopyridine ligand. *Dalton Trans.* **2016,** *45* (25), 10131-10135.
58. Colmer, H. E.; Howcroft, A. W.; Jackson, T. A., Formation, Characterization, and O–O Bond Activation of a Peroxomanganese(III) Complex Supported by a Cross-Clamped Cyclam Ligand. *Inorg. Chem.* **2016,** *55* (5), 2055-2069.
59. Barman, P.; Upadhyay, P.; Faponle, A. S.; Kumar, J.; Nag, S. S.; Kumar, D.; Sastri, C. V.; de Visser, S. P., Deformylation Reaction by a Nonheme Manganese(III)–Peroxo Complex via Initial Hydrogen-Atom Abstraction. *Angew. Chem. Int. Ed.* **2016,** *55* (37), 11091-11095.
60. Seo, M. S.; Kim, J. Y.; Annaraj, J.; Kim, Y.; Lee, Y.-M.; Kim, S.-J.; Kim, J.; Nam, W., [Mn(tmc)(O_2)]$^+$: A Side-On Peroxide Manganese(III) Complex Bearing a Non-heme Ligand. *Angew. Chem. Int. Ed.* **2007,** *46*, 377-380.
61. Shook, R. L.; Gunderson, W. A.; Greaves, J.; Ziller, J. W.; Hendrich, M. P.; Borovik, A. S., A monomeric Mn(III)-peroxo complex derived directly from dioxygen. *J. Am. Chem. Soc.* **2008,** *130* (28), 8888-9.
62. Kang, H.; Cho, J.; Cho, K. B.; Nomura, T.; Ogura, T.; Nam, W., Mononuclear manganese-peroxo and bis(mu-oxo)dimanganese complexes bearing a common N-methylated macrocyclic ligand. *Chemistry* **2013,** *19* (42), 14119-25.
63. Leto, D. F.; Chattopadhyay, S.; Day, V. W.; Jackson, T. A., Reaction landscape of a pentadentate N5-ligated Mn(II) complex with O2 - and H2O2 includes conversion of a

peroxomanganese(III) adduct to a bis(mu-oxo)dimanganese(III,IV) species. *Dalton Trans.* **2013,** *42* (36), 13014-25.

64. Singh, U. P.; Sharma, A. K.; Hikichi, S.; Komatsuzaki, H.; Moro-oka, Y.; Akita, M., Hydrogen bonding interaction between imidazolyl N–H group and peroxide: Stabilization of Mn(III)-peroxo complex TpiPr2Mn(η2-O2)(imMeH) (imMeH=2-methylimidazole). *Inorg. Chim. Acta* **2006,** *359* (13), 4407-4411.
65. Denler, M. C.; Wijeratne, G. B.; Rice, D. B.; Colmer, H. E.; Day, V. W.; Jackson, T. A., Mn(III)-Peroxo adduct supported by a new tetradentate ligand shows acid-sensitive aldehyde deformylation reactivity. *Dalton Trans.* **2018,** *47* (38), 13442-13458.
66. Sankaralingam, M.; Lee, Y.-M.; Jeon, S. H.; Seo, M. S.; Cho, K.-B.; Nam, W., A mononuclear manganese(iii)–hydroperoxo complex: synthesis by activating dioxygen and reactivity in electrophilic and nucleophilic reactions. *Chem. Commun.* **2018,** *54* (10), 1209-1212.
67. So, H.; Park, J.-H.; Cho, K.-B.; Lee, Y.-M.; Seo, M. S.; Cho, J.; Sarangi, R.; Nam, W., Spectroscopic Characterization and Reactivity Studies of a Mononuclear Nonheme Mn(III)−Hydroperoxo Complex. *J. Am. Chem. Soc.* **2014,** *136*, 12229−12232.
68. Lin, Y. H.; Kutin, Y.; van Gastel, M.; Bill, E.; Schnegg, A.; Ye, S.; Lee, W. Z., A Manganese(IV)-Hydroperoxo Intermediate Generated by Protonation of the Corresponding Manganese(III)-Superoxo Complex. *J. Am. Chem. Soc.* **2020,** *142* (23), 10255-10260.
69. Lin, Y. H.; Cramer, H. H.; van Gastel, M.; Tsai, Y. H.; Chu, C. Y.; Kuo, T. S.; Lee, I. R.; Ye, S.; Bill, E.; Lee, W. Z., Mononuclear Manganese(III) Superoxo Complexes: Synthesis, Characterization, and Reactivity. *Inorg. Chem.* **2019,** *58* (15), 9756-9765.
70. Opalade, A. A.; Parham, J. D.; Day, V. W.; Jackson, T. A., Characterization and chemical reactivity of room-temperature-stable Mn(III)-alkylperoxo complexes. *Chem. Sci.* **2021,** *12* (38), 12564-12575.
71. Coggins, M. K.; Martin-Diaconescu, V.; DeBeer, S.; Kovacs, J. A., Correlation between structural, spectroscopic, and reactivity properties within a series of structurally analogous metastable manganese(III)-alkylperoxo complexes. *J. Am. Chem. Soc.* **2013,** *135* (11), 4260-72.
72. Coggins, M. K.; Kovacs, J. A., Structural and spectroscopic characterization of metastable thiolate-ligated manganese(III)-alkylperoxo species. *J. Am. Chem. Soc.* **2011,** *133* (32), 12470-3.
73. Parham, J. D.; Wijeratne, G. B.; Rice, D. B.; Jackson, T. A., Spectroscopic and Structural Characterization of Mn(III)-Alkylperoxo Complexes Supported by Pentadentate Amide-Containing Ligands. *Inorg. Chem.* **2018,** *57* (5), 2489-2502.
74. Rice, D. B.; Wijeratne, G. B.; Burr, A. D.; Parham, J. D.; Day, V. W.; Jackson, T. A., Steric and Electronic Influence on Proton-Coupled Electron-Transfer Reactivity of a Mononuclear Mn(III)-Hydroxo Complex. *Inorg. Chem.* **2016,** *55* (16), 8110-20.
75. Stoll, S.; Schweiger, A., EasySpin, a comprehensive software package for spectral simulation and analysis in EPR. *J Magn Reson* **2006,** *178* (1), 42-55.
76. Ravel, B.; Newville, M., ATHENA, ARTEMIS, HEPHAESTUS: data analysis for X-ray absorption spectroscopy using IFEFFIT. *J. Synchrotron Radiat.* **2005,** *12* (Pt 4), 537-41.
77. Sankaralingam, M.; Jeon, S. H.; Lee, Y.-M.; Seo, M. S.; Ohkubo, K.; Fukuzumi, S.; Nam, W., An amphoteric reactivity of a mixed-valent bis(μ-oxo)dimanganese(iii,iv) complex acting as an electrophile and a nucleophile. *Dalton Trans.* **2016,** *45* (1), 376-383.

78. Wojdyr, M., Fityk: a general-purpose peak fitting program. *J. Appl. Crystallogr.* **2010,** *43* (5 Part 1), 1126-1128.
79. Neese, F., The ORCA program system. *WIREs Computational Molecular Science* **2011,** *2* (1), 73-78.
80. Buhl, M.; Kabrede, H., Geometries of Transition-Metal Complexes from Density-Functional Theory. *J. Chem. Theory Compu.t* **2006,** *2* (5), 1282-90.
81. Weigend, F.; Ahlrichs, R., Balanced basis sets of split valence, triple zeta valence and quadruple zeta valence quality for H to Rn: Design and assessment of accuracy. *Phys. Chem. Chem. Phy.s* **2005,** *7* (18), 3297-305.
82. Weigend, F., Accurate Coulomb-fitting basis sets for H to Rn. *Phys. Chem. Chem. Phys.* **2006,** *8* (9), 1057-65.
83. Neese, F., An improvement of the resolution of the identity approximation for the formation of the Coulomb matrix. *J. Comput. Chem.* **2003,** *24* (14), 1740-7.
84. Perdew, J. P.; Tao, J.; Staroverov, V. N.; Scuseria, G. E., Meta-generalized gradient approximation: explanation of a realistic nonempirical density functional. *J. Chem. Phys.* **2004,** *120* (15), 6898-911.
85. Perdew, J. P.; Kurth, S.; Zupan, A.; Blaha, P., Accurate Density Functional with Correct Formal Properties: A Step Beyond the Generalized Gradient Approximation. *Phys. Rev. Lett.* **1999,** *82* (12), 2544-2547.
86. Marenich, A. V.; Cramer, C. J.; Truhlar, D. G., Universal solvation model based on solute electron density and on a continuum model of the solvent defined by the bulk dielectric constant and atomic surface tensions. *J. Phys. Chem. B* **2009,** *113* (18), 6378-96.
87. Lee, C.; Yang, W.; Parr, R. G., Development of the Colle-Salvetti correlation-energy formula into a functional of the electron density. *Phys. Rev. B Condens Matter* **1988,** *37* (2), 785-789.
88. Hellweg, A.; Hättig, C.; Höfener, S.; Klopper, W., Optimized accurate auxiliary basis sets for RI-MP2 and RI-CC2 calculations for the atoms Rb to Rn. *Theor. Chem. Acc.* **2007,** *117* (4), 587-597.
89. Izsak, R.; Neese, F., An overlap fitted chain of spheres exchange method. *J. Chem. Phys.* **2011,** *135* (14), 144105.
90. Neese, F.; Wennmohs, F.; Hansen, A.; Becker, U., Efficient, approximate and parallel Hartree–Fock and hybrid DFT calculations. A 'chain-of-spheres' algorithm for the Hartree–Fock exchange. *Chem. Phys.* **2009,** *356* (1-3), 98-109.
91. Angeli, C.; Cimiraglia, R.; Malrieu, J.-P., n-electron valence state perturbation theory: A spinless formulation and an efficient implementation of the strongly contracted and of the partially contracted variants. *J. Chem. Phys.* **2002,** *117* (20), 9138-9153.
92. Angeli, C.; Cimiraglia, R.; Malrieu, J.-P., N-electron valence state perturbation theory: a fast implementation of the strongly contracted variant. *Chem. Phys. Lett.* **2001,** *350* (3-4), 297-305.
93. Angeli, C.; Cimiraglia, R.; Evangelisti, S.; Leininger, T.; Malrieu, J. P., Introduction of n-electron valence states for multireference perturbation theory. *J. Chem. Phys.s* **2001,** *114* (23), 10252-10264.
94. Wijeratne, G. B.; Corzine, B.; Day, V. W.; Jackson, T. A., Saturation kinetics in phenolic O-H bond oxidation by a mononuclear Mn(III)-OH complex derived from dioxygen. *Inorg. Chem.* **2014,** *53* (14), 7622-34.

95. Lee, Y.; Jackson, T. A., Ligand Influence on Structural Properties and Reactivity of Bis(μ-oxo)dimanganese(III,IV) Species and Comparison of Reactivity with Terminal MnIV-oxo Complexes. *ChemistrySelect* **2018,** *3* (47), 13507-13516.
96. Hureau, C.; Blondin, G.; Charlot, M.-F.; Philouze, C.; Nierlich, M.; Cesario, M.; Anxolabehere-Mallart, E., Synthesis, Structure, and Characterization of New Mononuclear Mn(II) Complexes. Electrochemical Conversion into New Oxo-Bridged Mn_2(III,IV) Complexes. Role of Chloride Ions. *Inorg. Chem.* **2005,** *44* (10), 3669-3683.
97. Goodson, P. A.; Glerup, J.; Hodgson, D. J.; Michelsen, K.; Pedersen, E., Binuclear bis(.mu.-oxo)dimanganese(III,IV) and -(IV,IV) complexes with N,N'-bis(2-pyridylmethyl)-1,2-ethanediamine. *Inorg. Chem.* **1990,** *29* (3), 503-508.
98. Chen, H.; Tagore, R.; Das, S.; Incarvito, C.; Faller, J. W.; Crabtree, R. H.; Brudvig, G. W., General Synthesis of Di-μ-oxo Dimanganese Complexes as Functional Models for the Oxygen Evolving Complex of Photosystem II. *Inorg. Chem.* **2005,** *44* (21), 7661-7670.
99. Franke, A.; Fertinger, C.; van Eldik, R., Axial ligand and spin-state influence on the formation and reactivity of hydroperoxo-iron(III) porphyrin complexes. *Chem. Eur. J.* **2012,** *18* (22), 6935-49.
100. Xu, S.; Draksharapu, A.; Rasheed, W.; Que, L., Jr., Acid pKa Dependence in O-O Bond Heterolysis of a Nonheme Fe(III)-OOH Intermediate To Form a Potent Fe(V) horizontal lineO Oxidant with Heme Compound I-Like Reactivity. *J. Am. Chem. Soc.* **2019,** *141* (40), 16093-16107.
101. Rice, D. B.; Jones, S. D.; Douglas, J. T.; Jackson, T. A., NMR Studies of a Mn(III)-hydroxo Adduct Reveal an Equilibrium between Mn(III)-hydroxo and mu-Oxodimanganese(III,III) Species. *Inorg. Chem.* **2018,** *57* (13), 7825-7837.
102. Rice, D. B.; Munasinghe, A.; Grotemeyer, E. N.; Burr, A. D.; Day, V. W.; Jackson, T. A., Structure and Reactivity of (mu-Oxo)dimanganese(III,III) and Mononuclear Hydroxomanganese(III) Adducts Supported by Derivatives of an Amide-Containing Pentadentate Ligand. *Inorg. Chem.* **2019,** *58* (1), 622-636.
103. Rice, D. B.; Wijeratne, G. B.; Jackson, T. A., Mn K-edge X-ray absorption studies of mononuclear Mn(III)-hydroxo complexes. *J. Biol. Inorg. Chem.* **2017**, *22*, 1281-1293.
104. Massie, A. A.; Kostopoulos, N.; Grotemeyer, E. N.; Noël, J.-M.; Jackson, T. A.; Anxolabéhère-Mallart, E., Electrochemical Formation and Reactivity of a Mn-Peroxo Complex Bearing an Amido N5 Ligand. *ChemElectroChem* **2022,** *9* (11), e202200112.
105. Lionetti, D.; Suseno, S.; Tsui, E. Y.; Lu, L.; Stich, T. A.; Carsch, K. M.; Nielsen, R. J.; Goddard, W. A.; Britt, R. D.; Agapie, T., Effects of Lewis Acidic Metal Ions (M) on Oxygen-Atom Transfer Reactivity of Heterometallic Mn3MO4 Cubane and Fe3MO(OH) and Mn3MO(OH) Clusters. *Inorg. Chem.* **2019,** *58* (4), 2336-2345.
106. Geiger, R. A.; Chattopadhyay, S.; Day, V. W.; Jackson, T. A., Nucleophilic reactivity of a series of peroxomanganese(III) complexes supported by tetradentate aminopyridyl ligands. *Dalton Trans.* **2011,** *40* (8), 1707-15.
107. Cantu Reinhard, F. G.; Barman, P.; Mukherjee, G.; Kumar, J.; Kumar, D.; Kumar, D.; Sastri, C. V.; de Visser, S. P., Keto-Enol Tautomerization Triggers an Electrophilic Aldehyde Deformylation Reaction by a Nonheme Manganese(III)-Peroxo Complex. *J. Am. Chem. Soc.* **2017,** *139* (50), 18328-18338.
108. Cho, J.; Jeon, S.; Wilson, S. A.; Liu, L. V.; Kang, E. A.; Braymer, J. J.; Lim, M. H.; Hedman, B.; Hodgson, K. O.; Valentine, J. S.; Solomon, E. I.; Nam, W., Structure and

reactivity of a mononuclear non-haem iron(III)-peroxo complex. *Nature* **2011,** *478* (7370), 502-505.

109. Kim, Y. M.; Cho, K. B.; Cho, J.; Wang, B.; Li, C.; Shaik, S.; Nam, W., A mononuclear non-heme high-spin iron(III)-hydroperoxo complex as an active oxidant in sulfoxidation reactions. *J. Am. Chem. Soc.* **2013,** *135* (24), 8838-41.
110. Park, M. J.; Lee, J.; Suh, Y.; Kim, J.; Nam, W., Reactivities of mononuclear non-heme iron intermediates including evidence that lron(III) - Hydroperoxo species is a sluggish oxidant. *J. Am. Chem. Soc.* **2006,** *128* (8), 2630-2634.
111. Wegeberg, C.; Lauritsen, F. R.; Frandsen, C.; Morup, S.; Browne, W. R.; McKenzie, C. J., Directing a Non-Heme Iron(III)-Hydroperoxide Species on a Trifurcated Reactivity Pathway. *Chem. Eur. J.* **2018,** *24* (20), 5134-5145.
112. Liu, L. V.; Hong, S.; Cho, J.; Nam, W.; Solomon, E. I., Comparison of high-spin and low-spin nonheme Fe(III)-OOH complexes in O-O bond homolysis and H-atom abstraction reactivities. *J. Am. Chem. Soc.* **2013,** *135* (8), 3286-99.
113. Oloo, W. N.; Que, L., Jr., Bioinspired Nonheme Iron Catalysts for C-H and C horizontal lineC Bond Oxidation: Insights into the Nature of the Metal-Based Oxidants. *Acc. Chem. Res.* **2015,** *48* (9), 2612-21.
114. Serrano-Plana, J.; Acuna-Pares, F.; Dantignana, V.; Oloo, W. N.; Castillo, E.; Draksharapu, A.; Whiteoak, C. J.; Martin-Diaconescu, V.; Basallote, M. G.; Luis, J. M.; Que, L., Jr.; Costas, M.; Company, A., Acid-Triggered O-O Bond Heterolysis of a Nonheme Fe(III)(OOH) Species for the Stereospecific Hydroxylation of Strong C-H Bonds. *Chem. Eur. J.* **2018,** *24* (20), 5331-5340.
115. Cho, J.; Sarangi, R.; Nam, W., Mononuclear metal-O2 complexes bearing macrocyclic N-tetramethylated cyclam ligands. *Acc. Chem. Res.* **2012,** *45* (8), 1321-30.
116. Parham, J. D.; Wijeratne, G. B.; Mayfield, J. R.; Jackson, T. A., Steric control of dioxygen activation pathways for MnII complexes supported by pentadentate, amide-containing ligands. *Dalton Trans.* **2019,** *48* (34), 13034-13045.